KU LEUVEN

Faculty of Science

Resonance scattering of ^{12}C nuclei on protons in the Maya active target

Mohammad KHODERY

Supervisor: Prof. R. Raabe
Co-supervisor: Sara Sambi

Thesis presented in
fulfillment of the requirements
for the degree of Master of Science
in Nuclear Physics

Academic year 2012-2013

Summary

This work is related to the realm of exotic nuclei. These are nuclei that exist far from the valley of stability. Study of these nuclei introduced many interesting phenomena and changed our understanding about the nuclear structure. As exotic nuclei are very short lived, their study has to be at the time of their production using radioactive beams of the exotic nuclei.

The goal of the experiment was to study the ^{13}Be low-lying energy levels. The experiment was performed at ISOLDE at CERN as ^{12}Be beams are produced at this facility with suitable intensity and energy. The method used to study ^{13}Be was elastic resonance reactions. This is a powerful tool to study unbound states.

This thesis concentrates on the ^{12}C nuclei that are present in the beam as isobaric contamination. ^{12}C in the beam is scattered on the protons which is the target. The protons are introduced in the form of isobutene gas. The aim of this work is to prove the principle of the technique of elastic resonance scattering in inverse kinematics performed in an active target detector. This is first of a kind experiment that uses the reconstruction of kinematics to measure events outside the 0^0 degree. The active target used in this experiment is called MAYA. This is a gaseous detector based on working principle of the time projection chamber TPC.

The analysis of the measurements starts with calibration of various components of MAYA detector. The next step is to identify different particles that are produced in the reaction. The reconstruction of the kinematics is later performed using the information obtained from MAYA to show the lab and center of mass spectra of the ^{13}N compound nucleus which is produced by the scattering of ^{12}C nuclei on protons.

The thesis concludes with a discussion about the outcome of the measurement and the advantages of using active targets for reconstruction of kinematics. The possible improvement of the setup is also given and the future possibilities of using MAYA in more experiments.

Samenvatting

Dit werk heeft betrekking op het gebied van exotische kernen. Dit zijn kernen die bestaan ver van de vallei van stabiliteit. Studie van deze kernen introduceerde vele interessante fenomenen en veranderde ons begrip over de nucleaire structuur. Aangezien exotische kernen een zeer korte levensduur hebben, moet hun studie gebeuren op het moment van hun productie met behulp van radioactieve straling van deze exotische kernen.

Het doel van het experiment was om de ^{13}Be laaggelegen energieniveaus te bestuderen. Het experiment werd uitgevoerd bij ISOLDE in CERN, aangezien deze faciliteit 12BE stralen produceert met geschikte intensiteit en energie. De methode die wordt gebruikt om ^{13}Be studeren was via elastische resonantie reacties. Dit is een krachtig hulpmiddel om niet-gebonden toestanden te bestuderen.

Dit proefschrift concentreert zich op de ^{12}C kernen die in de bundle als isobare verontreiniging optreden. ^{12}C in de bundel wordt verstrooid door de protonen in de trefschijf. De protonen worden geïntroduceerd in de vorm van isobuteen gas. Het doel van dit werk is om het principe van de techniek van elastische resonantie verstrooiing in inverse kinematica uitgevoerd in een actieve doeldetektor te bewijzen. Dit is het eerste experiment van zijn soort dat de reconstructie van de kinematica gebruikt om gebeurtenissen buiten de 0^0 graden te meten. De werkzame trefschijf in dit experiment wordt MAYA genoemd. Dit is een gasvormige detector gebaseerd op werkingsprincipe van de tijd projectie kamer TPC.

De analyse van de metingen begint met kalibratie van diverse onderdelen van Maya detector. De volgende stap is om verschillende deeltjes die worden geproduceerd in de reactie te identificeren. De reconstructie van de kinematiek wordt later uitgevoerd met de informative verkregen met MAYA. Deze informative wordt omgezet naar spectra van de gebonden ^{13}N kern in het ten opzichte van het laboratoriumsysteem en het massacentrumsysteem. ^{13}N wordt geproduceerd door de verstrooiing van ^{12}C kernen op de protonen.

Het proefschrift eindigt met een discussie over de uitkomst van de metingen en de voordelen van het gebruik van actieve doelen voor de wederopbouw van de kinematica. De mogelijke verbetering van de setup wordt ook gegeven en de toekomstige mogelijkheden van het gebruik MAYA in verdure experimenten wordt besproken.

Contents

Word of Thanks

This thesis could not have been made without the help and support of many. I would like to extend my sincere gratitude to all those who made it possible.

In the first place, I would like to thank Prof. Dr. Riccardo Raabe for giving me the opportunity to join his team, for his kind supervision and for his time given to me when needed. I would also like to thank Sara Sambi for all the help and effort in guiding me through this thesis. I really appreciate her willing to help me solving my problems or explaining them.

Big thanks also for all the researchers in my office who always were willing to give all the guidance I needed. They were really of great support.

Finally I thank all professors in nuclear spectroscopy group, Mark Huyse and Piet Van Duppen. All IKS members and all fellow students who made it fun atmosphere to work.

Leuven,
August 2013

Chapter 1 Introduction

In this chapter, we give a general introduction about the nuclear structure. We also show some of the new features discovered as we approach the boundaries of nuclear landscape. The motivation of this work is then addressed. At the end of the chapter, some theoretical and experimental aspects are reviewed.

1.1 Nuclear structure

The picture of the nuclear atom which consists of a tiny positive mass in its center surrounded by electrons was the result of famous Rutherford experiment of alpha particles on thin sheet of gold. It was his experiment that provided a new branch of science, nuclear physics [1].

Nuclear physics deals with the properties of the nucleus, and the laws governing the structure of nuclei. The nucleus in its simplest picture is made of protons and neutrons. These are called nucleons. A nucleus is characterized by the total number of protons Z, which is called the atomic number. Two nuclei with the same number of protons but with a different number of neutrons N are called isotopes. Therefore, the nucleus is also characterized by the total number of nucleons A (= Z + N) which is called the mass number. To denote a nucleus with Z protons and A-nucleons, the notation ${}^{A}_{Z}\mathrm{X}$ is used, where X is the name given to the nucleus.

A map of the territory of nuclear physics is drawn by positioning all the nuclei on a two dimensional N-Z grid, where the number of neutrons N is on the x-axis and the number of protons Z is on the y-axis. This nuclear landscape is the chart of nuclides (see fig. 1.1)

Today, more than 3000 nuclei have been observed and only 284 of them are stable. The boundaries of the chart of the nuclides introduce the concept of drip lines. Nuclear existence is limited on the neutron-rich side of the chart by the so called neutron drip line while it is limited by the proton drip line on the proton-rich side.

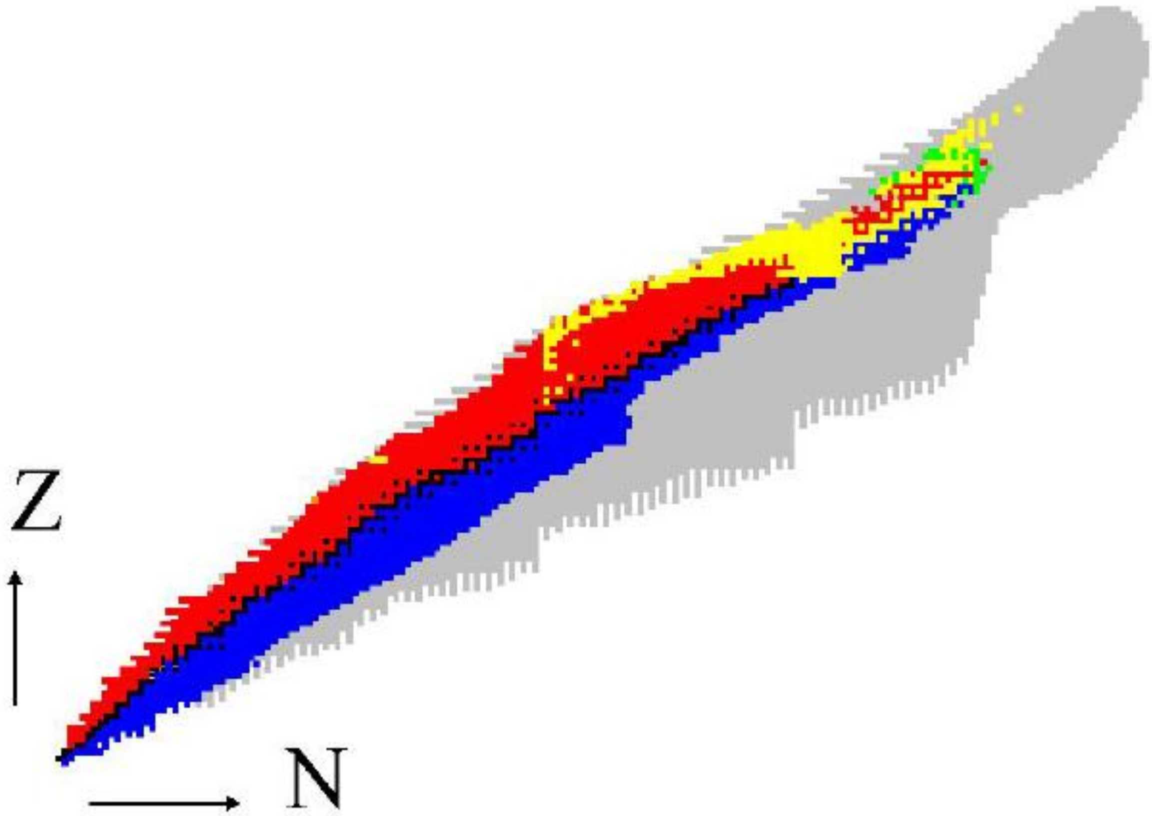

Figure 1.1: The nuclear chart. The different colors represent the decay modes (blue: $\boldsymbol{\beta}^{-}$ decay, red: $\boldsymbol{\beta}^{+}$decay / electron capture, yellow alpha decay and green spontaneous fission). The nuclei in grey are not observed experimentally but they are theoretically predicted to exist.

To find the location of the drip line, the separation energy is required. Neutron separation energy $\boldsymbol{S_n}$ is defined as the amount of energy required to remove a neutron from a nucleus. Similarly the proton separation energy S_p is defined [1].

$$S_n = B({}^{A}_{Z}X_N) - B({}^{A-1}_{Z}X_{N-1}) \tag{1}$$

$$S_p = B({}^{A}_{Z}X_N) - B({}^{A-1}_{Z-1}X_N) \tag{2}$$

where *B* is the binding energy of the nucleus.

Positive separation energy means that the nucleus is stable against nucleon emission. As neutrons are continuously added to a nucleus, the neutron separation energy approaches zero and the newly formed nucleus will immediately decay by neutron emission, that is the nucleus is unbound and the neutrons drip out of the nucleus.

The location of the neutron drip line is not straightforward. Properties of the nuclear force influence the location of the drip line. For nuclei near the drip line, additional stability is provided by the pairing interaction between two neutrons. For example, ^{9}Li is bound but it cannot bind one more neutron and ^{10}Li is unbound. However, the pairing between the last two neutrons combined with ^{9}Li potential is enough to make ^{11}Li bound with very small two- neutron separation energy S_{2n} = 295 keV [27]. Similar effect occurs at the proton drip line. While the neutron drip line is reached experimentally only for the lightest nuclei, the proton drip line is relatively well established up to mass around 100.

1.2 The Shell Model

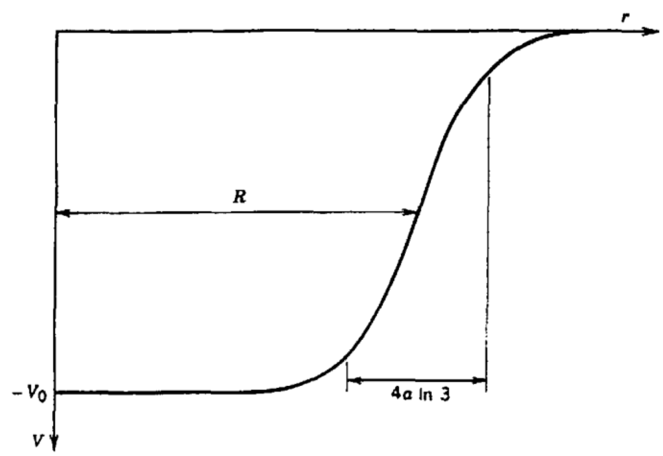

Figure 1.2: Realistic potential given by the formula $V(r) = \frac{-V_0}{1 + \exp[\frac{(r-R)}{a}]}$

Atomic theory based on a shell model provided remarkable success in revealing the complicated atomic structure. This tempted nuclear physicists to use a similar theory with the nucleus. Many experimental evidences supported the existence of nuclear shells. Measured proton and neutron separation energies showed sharp discontinuities in the separation energy similar to the atomic ionization energy for electrons. Certain number of protons and neutrons lead to more stable nuclei. These numbers (Z or N = 2, 8, 20, 28, 50, 82 and 126) represent the effect of filling a major shell. They are called the magic numbers [1].

However, this is immediately encountered by several differences. While electrons in the atom move in the central potential supplied by the nucleus, the nucleons move in a potential that they themselves created. While electrons move in orbits free of collisions, a well defined orbit for nucleons is difficult to imagine since the nucleon can make many collisions during each orbit.

The nuclear potential is obtained from the fundamental assumption of the shell model; the motion of a single nucleon is governed by a potential caused by all of the other nucleons. The existence of spatial orbits for nucleons depends on the Pauli Exclusion Principle which prohibits collisions between nucleons in the low lying levels when the higher levels are filled and cannot accept an additional nucleon [1].

Solving the Schrodinger equation for the realistic potential shown in fig.1.2 taking into account the spin orbit interaction produces the energy level scheme shown in fig. 1.3. The single-particle energy levels group into shells that are separated by large energy gaps which correspond to closed shells.

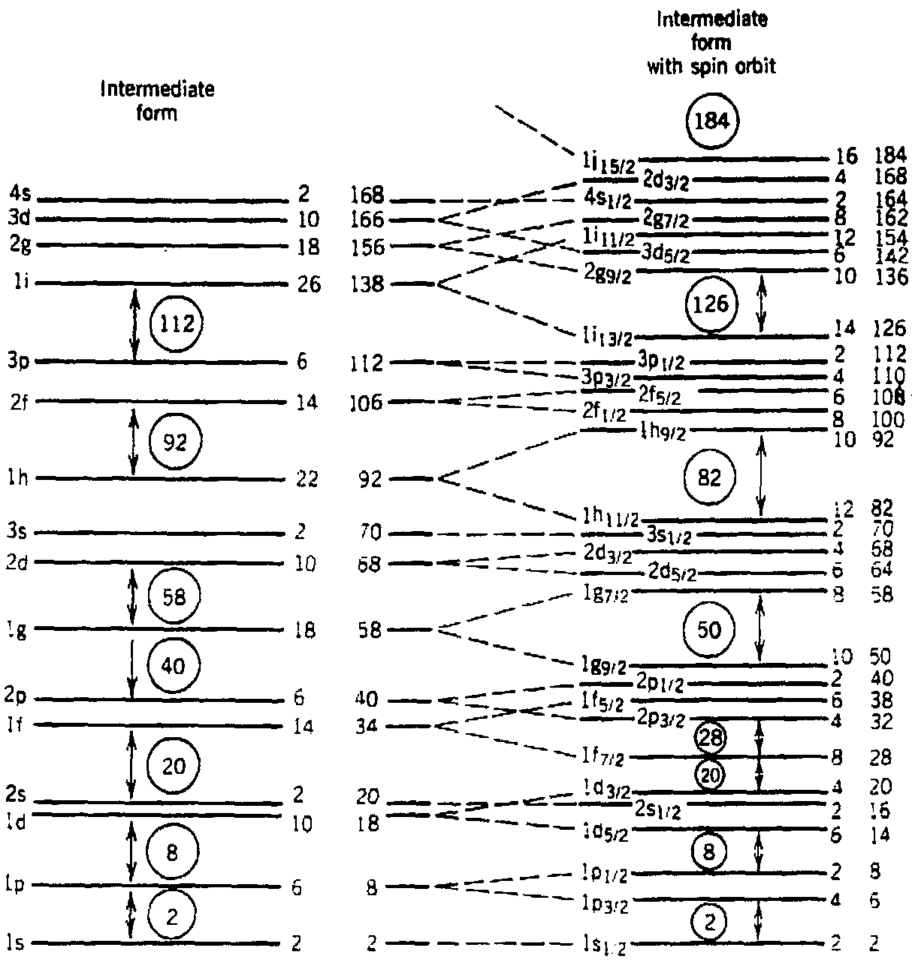

Figure 1.3: At the left the energy levels calculated from the realistic potential of fig. 1.2. At the right, the effect of the spin orbit interaction which splits the levels with $\boldsymbol{l} > 0$ into two levels. The shell effect is evident and the magic numbers are exactly reproduced [1].

By successively filling the neutrons and protons separately in the nuclear shells, the ground state of the nucleus is obtained. Nuclei can be excited by moving on or more nucleon to an orbital with higher energy.

1.3 Exotic Nuclei

Although the shell model is successful in explaining nuclear properties such as the appearance of the famous magic numbers, the nuclear spins and parities of different nuclear states and nuclear moments [1], it was not able to account for some new features discovered as we approach the neutron or proton drip lines. These exotic phenomena discovered far from the valley of stability are the drive for most of the experimental work recently.

One of such interesting phenomena is what we call the halo nucleus. Experiments showed that the nuclear matter density is not constant. The volume and mass number relation given by $r = r_0 A^{1/3}$ where $r_0 = 1.2\ fm$ is not valid for such nuclei. The excess nucleons in the halo give rise to large extensions in the wave functions or in other words, the probability of tunneling through the potential barrier is large. In some cases such as the two nucleon halo nucleus, pairing force will tend to form nucleon clusters allowed to be present at distances much larger than the normal radius of the nucleus. The nucleon-nucleon interaction at these distances is almost vanishing between the cluster and the core nucleus. This will give a dilute tail of nuclear matter and the result is a nucleus with large radius. ^{11}Li was the first and best-known example of halo nucleus discovered. It consists of a core of ^{9}Li surrounded by a cloud of two neutrons which give it large radius comparable to that of the lead nucleus [3-4].

Exotic nuclei with extreme neutron to proton ratio exhibit striking deviation from shell ordering that was seen in the shell model. New magic numbers appear and existing magic numbers in stable nuclei seems to be not valid far from stability. This is due to the fact that shell gaps are not persistent over the nuclear chart. Instead, new shell gaps lead to increased stability at different shell closure [5-6].

Another exotic feature occurs in the neutron rich Ne, Na and Mg near the region of N=20. The magic number N=20 seems to disappear. Promotion of neutron across N=20 occurs at surprisingly low energy leaving unoccupied single particle below. This region in the nuclear chart that includes isotopes whose ground states deviate from the normal shell structure is known as island of inversion [7-8].

Deformed nuclei have different shapes such as oblate or protlate shapes. However, in some cases different shapes can occur in the same nucleus for different excited states, a phenomenon known as shape coexistence [9]. Beyond proton drip line, the nuclei are not stable against proton emission [10]. Phenomena such as two-proton emission was observed and the mechanism behind is a hot topic of investigation.

These and other exotic features change our understanding of the nuclear structure, and trigger the search for new theoretical models of the nucleus. The systematic study of the exotic nuclei is essential for inspiring new nuclear models able to account for these findings. This systematic study is possible with the recent development in the radioactive ion beam RIB facilities [32].

1.4 Motivation

^{13}Be is an extremely exotic, unbound nucleus near the neutron drip line (see fig. 1.4) The experiment performed at ISOLDE aims at studying the ground state of ^{13}Be through the population of its isobaric analog resonance [13-15] in^{13}B using Maya active target detector. In this section , I describe first the motivation of this experimental work and then I focus on the work related to the topic of this master thesis, that is, resonance scattering of ^{12}C nuclei on protons in the Maya active target detector [12].

The experimental interest in the unbound system of ^{13}Be arises from the fact that it is a key nucleus towards the modeling two-neutron halo nucleus ^{14}Be. The energy scheme of the low lying energy states in ^{13}Be will also help to understand the evolution of the shell N=8 shell towards the neutron drip-line. Theoretical works concentrates on ^{13}Be or ^{12}Be + *n* interactions could be compared to the results from the low-lying states of ^{13}Be [13].

Resonance elastic scattering is the method used in this experiment to study ^{13}Be. It is a suitable experimental tool to study excited and unbound states [14]. The key point in this technique is that elastic resonance scattering has large cross section and dominates over all other possible reactions which could be a source of background. The competing reaction is the inelastic resonance scattering. We used a beam of ^{12}Be scattered on protons to populate the isobaric analog resonances of ^{13}Be in ^{13}B. Possible decay channels allowed by isospin conservation are the entrance channel (proton emission) and the conjugate channel (neutron emission).

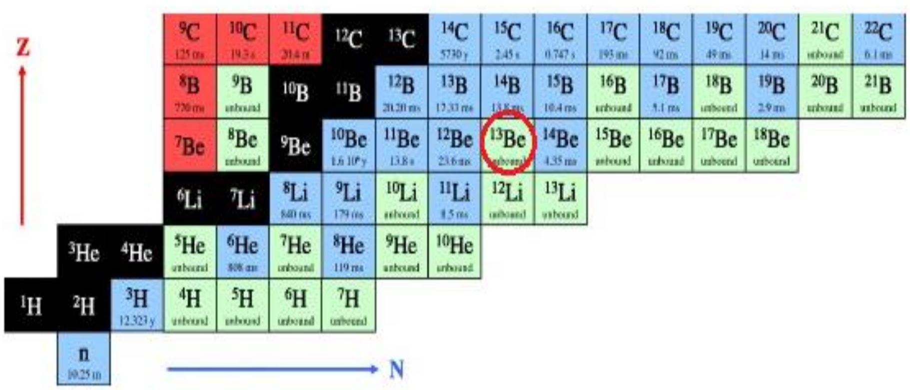

Figure 1.4: shows the location of the neutron-rich 13Be near the drip line.

^{12}Be beam produced at ISOLDE facility was contaminated by ^{12}C. The aim of the analysis is to use the ^{12}C events to prove the principle of the method of elastic resonance scattering in inverse kinematics using Maya active target. The analysis of ^{12}Be events is in the scope of the PhD of S. Sambi (PhD student).

The resonance scattering of ^{12}C on protons gives the compound nucleus ^{13}N. The part of ^{13}N level scheme that can be accessed in our experiment is shown in fig. 1.5.

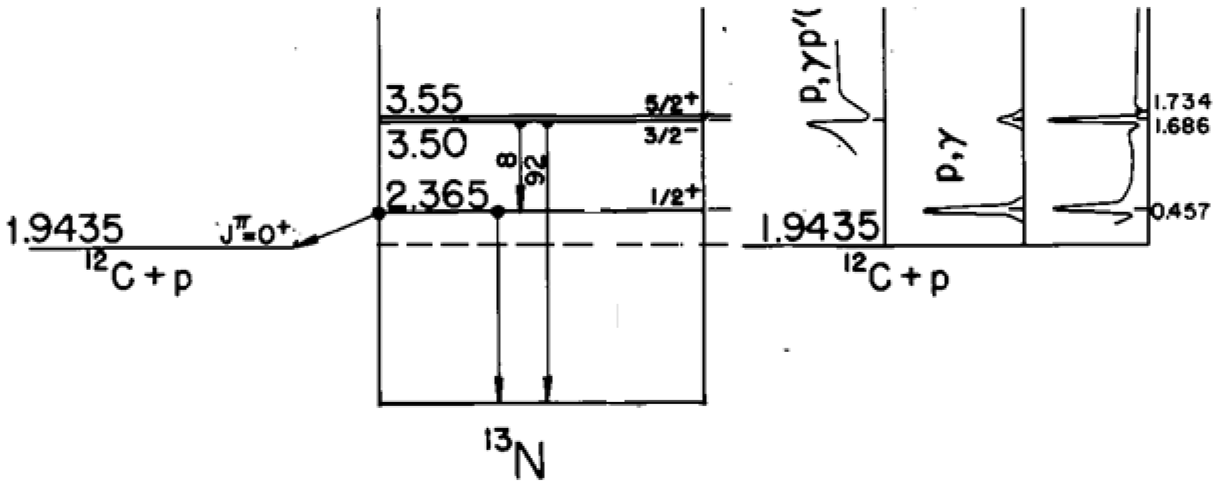

Figure 1.5: The part of the ^{13}N level scheme accessible in this experiment and the proton emission threshold.

1.5 Elastic resonance scattering

Resonance reactions is an intermediate type of interaction between the compound nucleus and direct reaction mechanisms. The model of compound nucleus regards unbound nuclear states as a continuum. Each state has a certain width and they are so close together that they overlap to form a continuum without structure, that is, unbound states are not discrete states. On the other hand, direct reactions are used to study bound states stable against particle emission, their width therefore are much smaller which allows us to treat them as discrete states. Resonance reactions are used to study discrete levels in the compound nucleus continuum. Resonances are unbound states with a finite lifetime even though they are above the particle emission threshold [1].

The occurrence of a resonant state in general originates from the quantum mechanical description of the process of a tunneling wave function. Resonance is an unbound state that exists for a finite time before its decay. The lifetime is related to the width of a state through the relation $\Gamma = \hbar/\tau$, where Γ is the width of the state and τ is the lifetime of that state. The potential well seen by the decaying nucleus determines the lifetime of that state. This is seen from the following reasoning: the transmission probability through a potential barrier is dependent on the height and width of the potential with respect to the energy of the state. The potential is essentially spherical which is added to it, an angular momentum barrier. In the case of a proton emission, a coulomb barrier is added as well. If the resonance state is located near the top of the potential where it can easily tunnel, the lifetime of that state is short. Whenever the tunneling is retarded, the lifetime will be longer and the state is a resonance [2].

Near the drip lines, nuclei have many unbound states and some interesting nuclei have no bound states at all. Beyond drip lines, nuclei by definition are unbound. They are unstable against particle emission which means that they will decay as soon as they are formed and therefore can only be probed as resonance states.

1.6 Methods of elastic scattering experiment

In the following sections, the different techniques used to perform elastic resonance scattering experiment are investigated.

1.6.1 Traditional solid thin target

Before Radioactive Ion Beam (RIB) facilities, elastic resonance scattering experiments were traditionally performed by bombarding a solid thin target with a light ion beam. The target is selected such that the interaction with the beam produces the compound nucleus to be investigated. The beam has a well-defined energy. To produce the excitation function, the beam energy needs to be changed in small steps of the order of keV to scan the resonances. Although this method gives high resolution excitation function, it is time consuming and not efficient for systematic study of exotic nuclei. It is also limited to regions close to the valley of stability as it is difficult to make a radioactive target of the few and short lived exotic nuclei. Generally in elastic resonance scattering using the conventional method of thin solid target, it is not possible to measure at 0^0 in the lab (180^0 in the center of mass system) because the scattered particles would interfere with the beam.

1.6.2 Thick Target

One way to circumvent the small energy steps is to use backscattering on a solid thick target [16]. The target slows down the beam and the reaction occurs at different depths corresponding to different energies which mean that a wide range of energy can be scanned with single beam energy. The energy range that could be scanned at once is given by the first excited state energy of the target nuclei[1] in order to distinguish between the elastic and inelastic scattering.

Another technique used to perform elastic resonance scattering experiment relies on the use of radioactive ion beams incident on a thick gas target [17]. This technique combines the high cross section associated with the elastic resonance scattering and efficient energy scanning of a thick target. To reach the drip line nuclei, it is easier to start with radioactive short-lived nuclei as the beam. Beams of radioactive nuclei incident on light targets is a natural solution and implies that elastic scattering is performed in inverse geometry.

The larger energy steps come at the expense of statistics because it is only possible now to measure at the 0^o in the lab (180^o in the center of mass system). This is because reconstruction of the kinematics will experience higher uncertainty in the determination of the interaction point or the vertex. Using a gas target, instead of solid one, brings greater flexibility into the measurement of the excitation function. By changing the gas pressure allows continuously changing the target thickness. Gas targets are also very homogenous.

1.6.3 Inverse kinematics

When elastic resonance scattering is combined with inverse kinematics, the beam is the heavy radioactive ion and the target is the light stable nuclei. In this way, nuclei at the drip lines could be reached in simple reactions.

Comparing the energy of the light particles in conventional and inverse kinematics, the detected energy of the light particles are about 4 times higher in inverse geometry. The gain in energy is advantageous in the case of resonances at low energies. The reaction products in inverse geometry are focused in the forward direction as a narrow cone rather than the case of traditional light beam on heavy target. This increases the detection efficiency as a larger solid angle could be covered.

[1] Since the light projectiles have higher excitation energy. protons don't have excited states and alpha particles first excited state at 20.210 MeV

Chapter 2 Experimental Setup

Our experiment was performed at ISOLDE facility located at CERN, where the very exotic ^{12}Be beam is produced and post-accelerated to the energy required by this experiment. This chapter deals with the experimental aspects of the beam production and detection setup used. We first introduce the general features of the RIB's production techniques. In the first section, brief description of the ISOLDE facility is given. The detection setup is then described in the next section. In the beam section, the characteristics of the ^{12}Be beam are described. Finally, the data acquisition carried out by the electronic modules is discussed.

2.1 The production of radioactive beams

The development in the field of Radioactive Ion Beams (RIB's) was a breakthrough in the investigation of exotic nuclei as it enabled us to access unexplored regions of the nuclear chart far from stability. There are two main techniques for the RIB's production: the "in-flight method" and the Isotope Separation On-Line (ISOL) technique. The latter was used for the production of ^{12}Be beam used in this experiment and will be described in detail.

In-flight technique for producing high energy RIB's relies on the forward focusing inherent in some nuclear reactions that occur when heavy projectiles at high incident energies (the primary beam) are incident on a light target. The exotic ions emerging from the reaction (the secondary beam) can then be separated- before they decay- from the primary beam and other reaction products by a combination of magnetic and electrostatic fields. Projectile fragmentation is an example of such reactions where beam is broken into smaller species retaining most of the momentum of the beam [31].

The ISOL technique relies on the availability of the radioactive species that are produced in a heavy target and then diffuse out. They are first ionized in an ion source. After extraction from the ion source, they are mass separated by a dipole magnet and finally post accelerated.

These different techniques provide beams with different properties, which make them complementary. The in-flight method provides beams of isotopes with very short half-lives but the quality is poor due to the kinetic energy spread in the reaction fragments. On the other hand, the ISOL technique is superior in beam quality but the production process depends on the chemical properties of the isotope at hand [31].

Short-lived isotopes can’t be obtained because the time required for the production process is longer. While with the in-flight separation technique, the beam is produced and delivered at high energies, ISOL technique is followed by post acceleration [18].

Production of exotic nuclei is confronted with many difficulties due to the extremely low cross section of the reactions used to produce them, overwhelming unwanted byproducts and extremely short half lives of the nuclei of interest. Production rate of the very exotic nuclei will always be marginal; therefore, transport of the produced isotopes to the detection setup must be efficient; otherwise one loses the few precious nuclei. For short-lived exotic nuclei, the losses due to radioactive decay between the moment of production and the arrival at the experimental set-up should be kept to a minimum. Unwanted species along with the nucleus of interest are called contaminants. If they have the same mass-over-charge ratio, they are called isobaric contaminants. Elimination of such contaminants requires an efficient separation process.

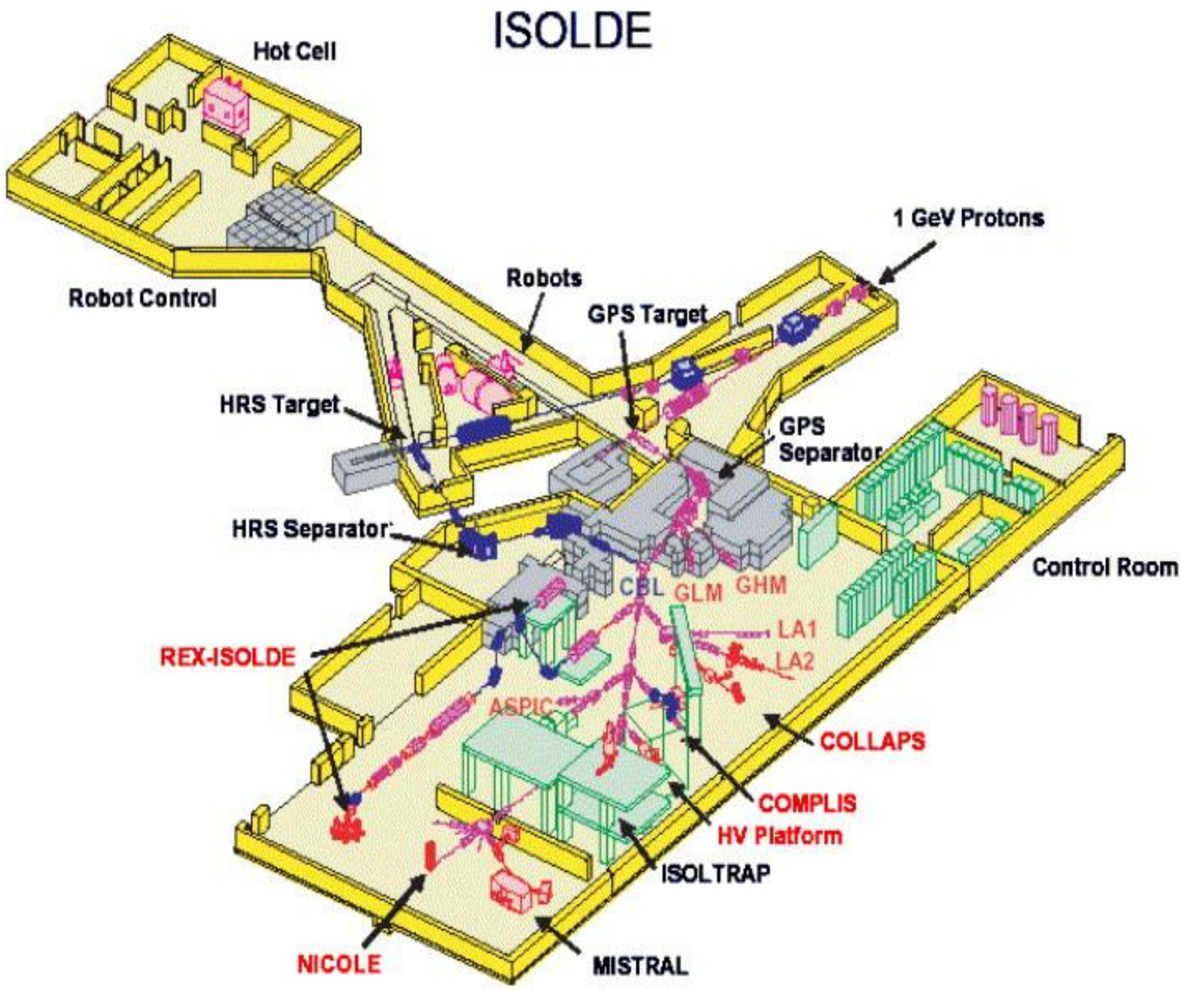

Figure 2.1: layout of the ISOLDE facility at CERN [19]

2.2 ISOLDE Facility

As mentioned before, the elastic resonance scattering experiment of the ^{12}Be on protons using MAYA active target detector was carried out at ISOLDE facility at CERN. It is an on-line mass separator able to produce a wide variety of radioactive ion beams. ISOLDE is the one of the few facilities that is able to provide a ^{12}Be of intensity and energy suitable for our experiment. The layout of the ISOLDE facility is shown in fig. 2.1. In the following section, main items are briefly introduced [18]

Production Target:

The 1.4 GeV protons beam from the CERN Proton Synchrotron Booster (PSB) impinges on a uranium carbide UC_x target to produce the radioactive ion beams of interest. Reaction mechanisms possible, when a high energy proton beam hits the target are fission, spallation and fragmentation. The advantages of this production method are the high cross section of the reaction and the high energy of the proton beam available.

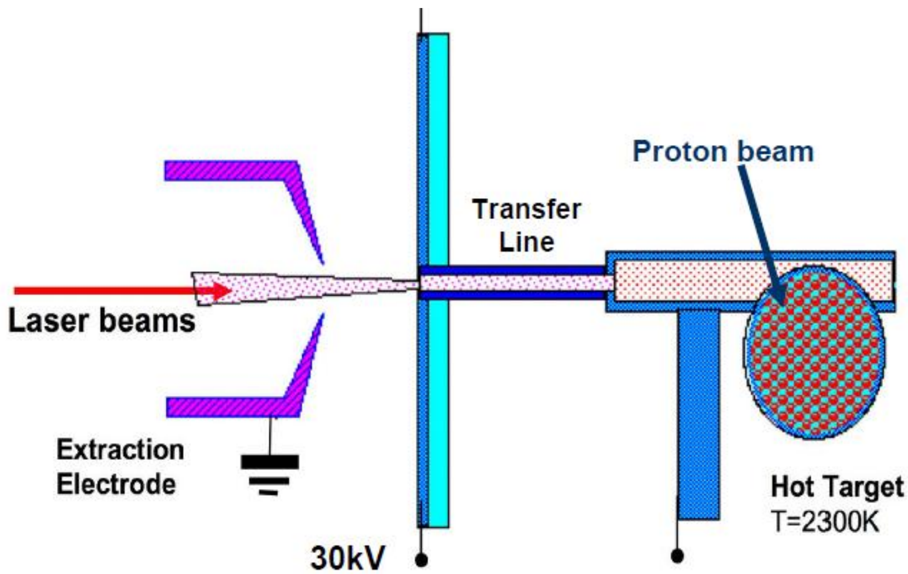

Figure 2.2 shows the target, transfer line and RILIS ion source

After their production, the reaction products diffuse out and effuse from the target to be transported to the ion source through a transfer line. The target, the transfer line and the ion source are kept at high temperature to reduce the diffusion time and to avoid lingering of the atoms to the walls of the line. Fig. 2.2 shows the target, transfer line and the ion source.

Ion Source:

Different ionization mechanisms are implemented at ISOLDE. The choice depends on the ionization potential of the element of interest, the required charge state and selectivity.
The ionization mechanism used in this experiment is called RILIS or Resonant Ionization Laser Ion Source. It is based stepwise excitation of atoms by laser photons to the continuum, or to auto-ionizing states, highly excited states close to the continuum. In the latter case the ionization step is achieved through infra-red irradiation, an electrical field or atomic collisions. The ionization process consists of typically two or three steps and, because of the resonant nature of most of these steps, resonant laser ionization is very efficient and chemically selective, resulting in isobarically and, if the laser bandwidth is narrow enough, isomerically pure beams. (See fig. 2.3)

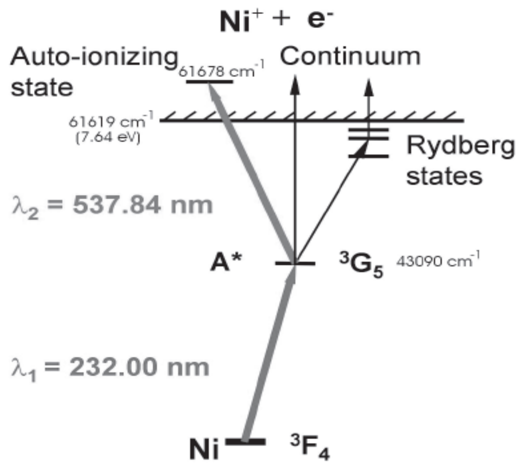

Figure 2.3 atomic level scheme showing the principle of resonant laser ionization of Ni.

Analyzing Magnet:

After extraction from the ion source by a DC potential difference between the ion source and an extraction electrode of around 60 keV, the low-energy ion beam is mass separated by an analyzing magnet and transported to the focal plane which is the ideal location along the beam line for focusing. Quality of the mass analyzing system is expressed by the mass resolving power which is defined by $R = M/\Delta\mathrm{M}$, where ΔM is the full width at half maximum of the beam spread in mass.

ISOLDE has two separators, the general purpose separator (GPS) with a mass resolving power of 2400 and the high resolution separator (HRS) which consists of two bending C-magnets with bending angles 60 and 90 degrees respectively with mass resolving power of 5000.

Post Acceleration:

This is achieved by cooling and bunching the ions in the buffer gas of a penning trap called REXTRAP followed by charge-state breeding in an Electron Beam Ion Source (EBIS) and post-acceleration in a linear accelerator.

For efficient and cost-effective operation of the linear accelerator, highly charged ions are required for injection. Therefore, a charge-state breeder is used. This is an Electron Beam Ion Source (EBIS), called REXEBIS that boost the 1+ ion beam to higher charge state. The EBIS obtains higher charge states through electron impact ionization under continuous bombardment with a highly dense electron beam.

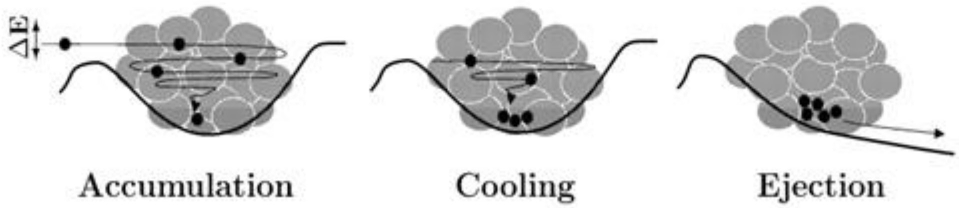

Figure 2.4 Steps of ion treatment in the penning trap before injected to the EBIS.

The EBIS requires a pulsed injection for operation; therefore the +1 ion beam is injected in a Penning trap called REXTRAP to bunch the ions prior to injection into the EBIS. In the trap the ions are accumulated and at the same time cooled via collisions with the buffer gas. See fig. 2.4. After a fixed time, which is determined by the required charge breeding time, the ion bunch is extracted from the penning trap and injected into the EBIS. The EBIS yield a pulsed beam.

The EBIS produces not only highly charged ions of the desired isotope in the desired charge state. Because of the residual gas present in the EBIS, a wide variety of highly charged residual gas ions emerge. The main contaminants are ^{12}C, ^{14}N, ^{15}N and ^{16}O. Therefore, a mass separator is placed after the EBIS which performs a mass to charge ratio separation by two bending-magnets.

The REX-LINAC post accelerator consists of 6 accelerating elements: a Radio-frequency quadrupole (RFQ), inter-digital H structure (HIS) and three seven gap resonators and a nine-gap resonator. REX-LINAC is able to accelerate up to 3 Mev/nucleon at the entrance of the setup. The REX-ISOLDE setup is shown in fig. 2.5.

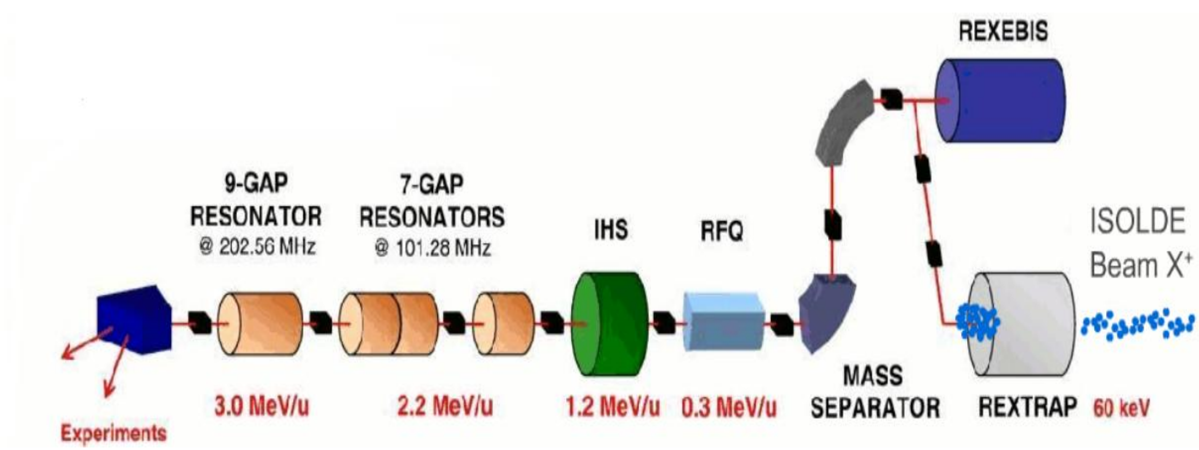

Figure 2.5 schematic drawings of REX-ISOLDE post-accelerator

2.3 Maya detector

2.3.1 Introduction to Active Targets

Active target detectors such as the bubble chamber were originally developed for high-energy physics, but it found its way to nuclear physics in the study of exotic nuclei far from the valley of stability. An active target detector is a gaseous ionization chamber where the gas serves as the target and the detection medium at the same time.

This type of detectors is based on the working principle of the time projection chamber TPC, where ionization electrons produced by charged particle in the filling gas, drift under the influence of the electric field applied over the volume of the gas to the anode wire where it produces an avalanche. The signals produced by the avalanches at the corresponding wires are used to build the projection of the particle track while the third dimension is deduced from the drift time of the avalanches.

The use of active target detector overcomes many of the difficulties encountered in the study of exotic nuclei. Because the target is also the detection gas; almost 100% detection efficiency is reached. This counterbalances the low production rates of the exotic nuclei. The thickness of the active target can be controlled by the pressure of the filling gas. The equivalent thickness can be increased until the beam is fully stopped within the target making full use of the limited production rate of exotic nuclei. Extremely low detection threshold allows the detection of low energy recoil particles which have or lose very low energy in the gas. An event-by-event reconstruction of kinematics enables us to extract information such as the position of the reaction vertex [20-21].

2.3.2 Maya Detector

The active target used in this experiment is called Maya. A schematic drawing of the external view is given in fig. 2.6.

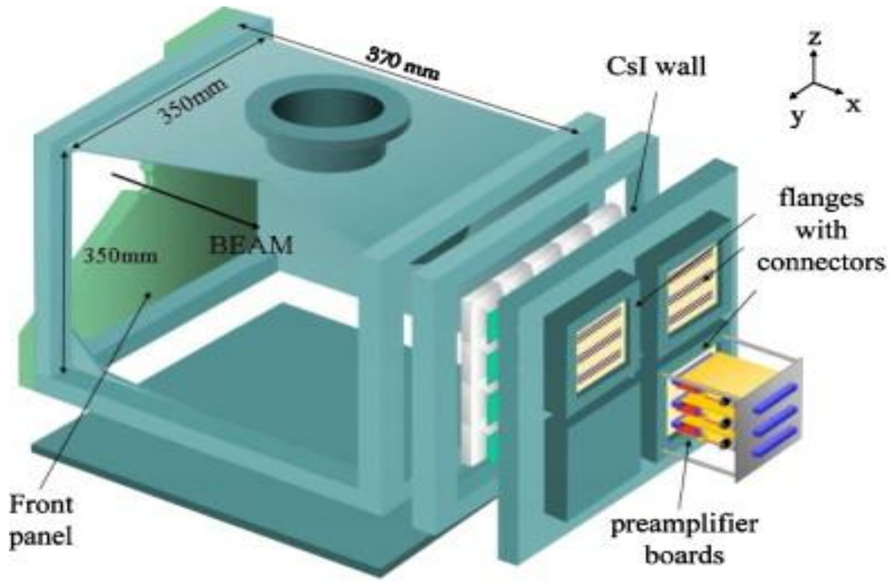

Figure 2.6 External view of Maya active target detector

The size of the detector is determined based on the design requirement of a reasonable drift time of the ionized electron cloud obtained by applying a reasonable bias voltage within 20 cm of maximum drift distance. The width is set to 25cm and the thickness is 28cm. These dimensions allow stopping most of the beams produced at SPIRAL facility at GANIL. The allowed operating pressure is limited to 3 atm [21].

Maya is divided into three zones, an active volume, a detection area and an ancillary detectors wall. A general layout of the detector showing the three zones is given in fig. 2.7.

The active volume is filled with the target gas where interactions between the beam and the gas take place. This volume is defined by the cathode plane at the top side, a Frisch grid at the bottom side that separates the active volume from the detection area. One side is the beam entrance and at the opposite side, the ancillary wall is placed. An electric field is applied between the cathode and the Frisch grid over the active volume. A cage of copper field strips is used to assure the homogeneity of the field.

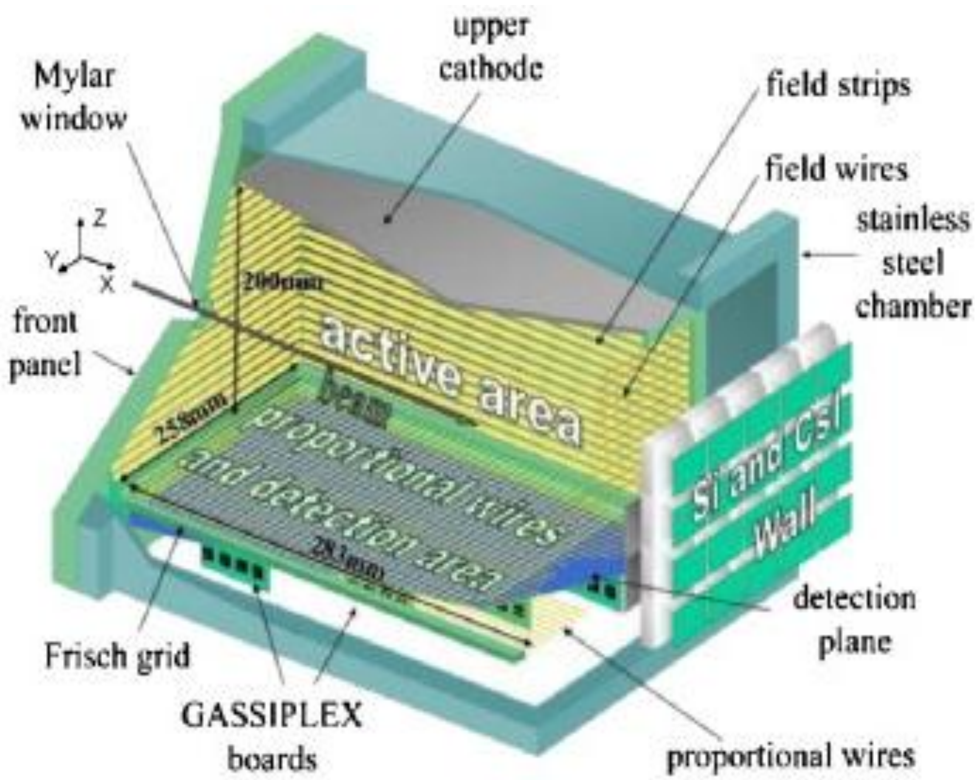

Figure 2.7 schematic internal view shows the 3 zones of the detector

The detection area is where the ionization electrons are amplified and recorded. The Frisch grid consists of Cu-Be wires perpendicular to the beam direction. Below the Frisch grid, at a modifiable distance, the anode wires are located. These are proportional wires parallel to the beam direction over which a high positive voltage is applied. The high electric field in the vicinity of the wires produces the amplification required through an avalanche triggered by the primary charge. The distance between the wires is also chosen to avoid interaction between neighboring wires or “cross talk”.

The function of the Frisch grid is to shield the amplification area and collects the positive ions produced at the anode wires that slowly drift in the opposite direction with respect to the electrons. A cathode plane below the anode wires plane is segmented in 37 x 35.5 mm side hexagonal pads forming 32x32 pads for charge collection. The charge on these pads is an image charge of the avalanches on the 32 proportional wires above and created through induction. The signals induced on the cathode pads are collected and delivered to the acquisition system by GASSIPLEX chips connected underneath the cathode board [21].

A small ionization chamber called “drift chamber” (DC) is placed between the active volume and the ancillary detectors wall. It is used for the localization of the crossing point of the recoil particle with a better spatial resolution than the array of solid state detectors placed behind the chamber itself. A schematic drawing of the layout of the DC is shown in fig. 2.8.

The ancillary detectors wall is used to detect the particles emitted in the forward direction which couldn’t be stopped in the active volume, especially light nuclei which lose only small fraction of their energy in the gas. The ancillary wall covers 45^0 around the beam for events in the middle of MAYA at around 15 cm. In this experiment, an array of 20 silicon detectors arranged in 4 rows of 5 detectors was used. Each detector is 700 um thick and area of 5 x 5 cm^2. Another array of 80 CsI detectors arranged in 8 rows of 10 detectors was placed behind the silicon array. Each CsI crystal is 1 cm thick and 2.5 x 2.5 cm^2 used.

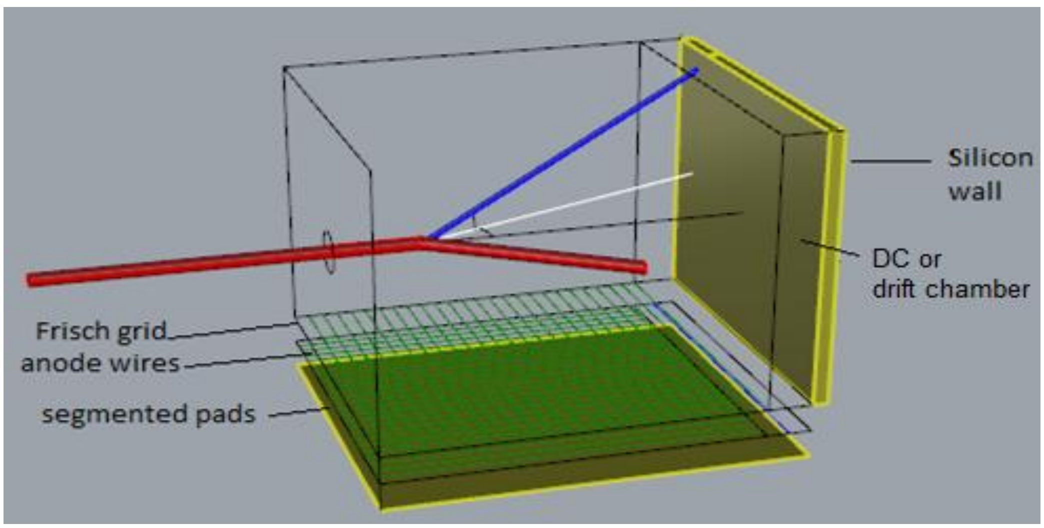

Figure 2.8 Schematic drawing of the drift chamber layout in front of the Silicon wall

Particle identification depends on the available information from Maya. If the particle is stopping in the gas, it could be identified using the unique relation between the energy of the particle and its range in a given gas according to the relation:

$$R \propto E^2/MZ^2$$

Where R is the range of the particle in the gas with energy E. M and Z are the mass and the atomic number of the particle.

For those particles stopped in the ancillary detectors wall, E-ΔE identification is possible. This technique is based on the measurement of the energy deposited in two detectors, the dirft chamber and the silicon wall. A particle will lose part of its energy in the drift chamber through ionization. The ion pairs produced are collected on an anode wire perpendicular to beam direction. The energy lost in the drift chamber is plotted against the total energy which is the sum of the energy loss and the energy measured in the silicon.

2.4 The Beam characteristics

The^{12}Be yield from uranium target bombardment with 2 µC protons was 7×10^3 particle/ µC. The intensity of the beam drops due to losses in the different stages up to the setup. Because the time structure of the beam and the particular nature of the setup which is a slow gaseous detector, Maya cannot accept high counting rates. It was difficult to estimate the absolute beam intensity. Fig.2.9 shows the signals produced by the ^{12}Be ions collected on an anode wire inside the gas detector. After a proton pulse, only the first few EBIS pulses contain ^{12}Be ions. The saturation of the signals could be seen in the right part of the fig. 2.9. A total of about 40-50 for each proton pulse was estimated.

The ^{12}Be beam produced at ISOLDE was highly contaminated by ^{12}C due to residual gas contamination inside the EBIS source. A stripper foil (thin carbon foil) was placed in our experiment after the EBIS. The function of this foil was to fully strip the $^{+}4$ ^{12}C from the EBIS and charge breed it to a $^{+}6$ state so that the mass separator after the EBIS can eliminate it through mass to charge ratio separation. The stripper reduced the amount of $^{+}4$ C by a factor of 45. Still, the number of ^{12}C per pulse was 10^4 times more than ^{12}Be. The ^{12}Be comprises less than 1% from the total intensity. The beam energy was set to 2.85 MeV/nucleon and EBIS mode was set to slow extraction.

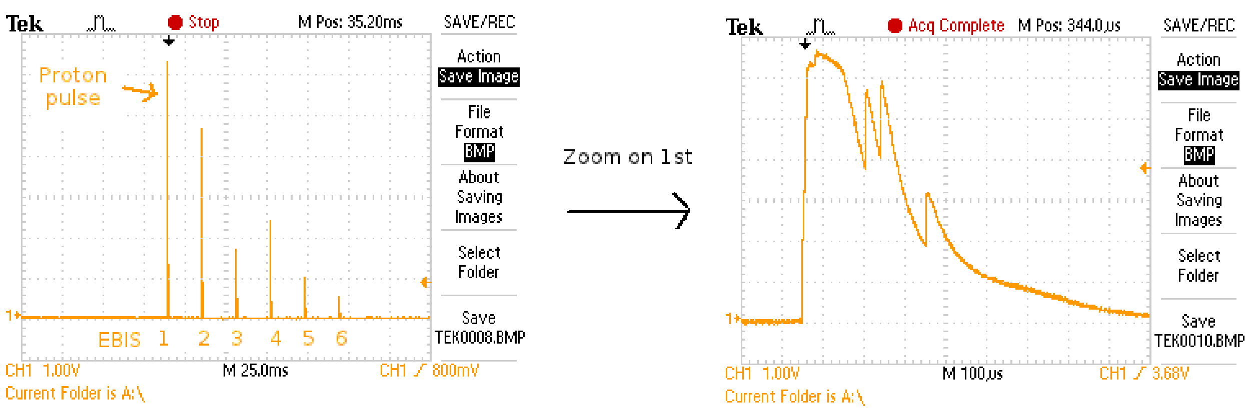

Figure 2.9: (left) Signals induced by the ^{12}Be on an anode wire in Maya. (right) the saturation of the signal due to each EBIS pulse.

To avoid the saturation of the data acquisition system by the ^{12}C high count rate, a modification was made to the detector during the measurement. An Aluminum mask was used to shield the ^{12}C tracks. This aluminum mask was placed above the Frisch grid stop the ionization electrons from reaching the anode wires. ^{12}Be tracks however, are longer and therefore can be seen on the cathode pads after the mask. Other tracks that could be seen are from protons that are scattered from the both of ^{12}C and ^{12}Be.

Isobutane (C_4H_{10}) was used as the filling gas and at the same time the proton target as contains 10 hydrogen atoms per molecule. The working pressure was set at the 160 mbar. This pressure was enough to stop the ^{12}Be beam with 2.85 MeV/nucleon before the silicon wall which is part of our detector. The voltage applied on the active volume of the detector was 3000V. This voltage is enough to obtain a reasonable drift time of 30 μs. 1500V bias voltage was applied on the anode wires to create a high electric field for amplification.

2.5 Electronics

2.5.1 The Trigger

The trigger for this experiment is affected by the nature of the beam delivered from REX-ISOLDE and the nature of Maya. The beam delivered to Maya was extremely contaminated with ^{12}C as explained. Furthermore, Maya is a slow gaseous detector that has to fully stop the beam and cannot accept high counting rates. For these reasons, the central anode wires collecting the charge of the incoming beam particles can't be used as a trigger because the carbon events would saturate the acquisition system and prevent recording the interesting ^{12}Be events. The ^{12}Be to ^{12}C ratio was estimated during the course of the measurements to be less than 1%. It is necessary therefore, to be able to select those few and precious ^{12}Be events from the overwhelming carbon events.

One way around the carbon signal on the wires was to shield the wires using aluminum mask. The pressure inside Maya is adjusted such that the ^{12}Be is stopped before the silicon wall by a suitable distance; this was done by increasing the pressure gradually until the ^{12}Be signal in the central silicon disappeared. At that pressure, SRIM simulations showed that the ^{12}C stopped at about 12 cm approximately from the entrance window. Using a 15 cm mask of Aluminum foil to cover the anode wires over the first half of Maya, would eliminate the carbon tracks. As the stopping power of the ^{12}Be is smaller than that of ^{12}C, Be-tracks are longer and allow the use of the signal on certain anode wires after the Aluminum mask as a trigger.

The trigger was built making use of the kinematics of the reaction. Since an elastically scattered proton would reach the silicon almost at the instant of the interaction. A proton hitting any of the silicon detectors is a suitable trigger. The silicon wall covers 45^0 degrees for events at the center of Maya at about 15 cm and most of the events due to the inverse kinematics are in the forward direction.

For events where the proton is scattered outside the silicon wall or it doesn't have enough energy to reach it, a signal on any of the lateral anode wires is a good trigger. Out of the 32 proportional wires, the central ones were disabled. These are the wires 16, 17, 18, and 19 which extend under the beam. This is to avoid triggering on the ^{12}Be ions.

2.5.2 The Logic

Ganil Master Trigger (GMT) is an electronic module which starts the data acquisition. When the GMT receives a trigger, it generates a *fast trigger analysis* (FTA) signal. The FTA signal starts the data readout by sending gates to the analogue to digital converter (ADC) and time to digital converter (TDC) modules to start recording within these gates. The gates have duration equal to the dead time (DT).

The electronic scheme shown in fig. 2.10 can be divided into 4 parts:

Silicon signal:
Silicon detectors provide energy measurement of the scattered protons. Signals from the 20 silicon detectors are sent to the preamplifier through which the bias voltage is applied. It is followed by a spectroscopy amplifier that gives two outputs. The amplified output signal corresponding to full charge collection is sent to the ADC, while the fast output signal is used after imposing a low threshold discrimination LTD as an external trigger in the GMT.

The anode wires:
Anode wires are used for energy and time measurement. The signal from each wire is pre-amplified and split into two signals. One is sent to the spectroscopic amplifier (SA) to measure the charge collected on each wire and sent to the acquisition thorough the ADC module.

The other branch is sent to a CFD constant fraction discriminator after which it is fed both to the Retard et Duree Variable (RDV) which is a module that apply a variable delay on the input signal and the Logic OR gate of the wires which is used without delay as a trigger to the GMT.

The trigger from wires is first validated by an AND gate with the inverse of the dead time $\overline{DT}$, allowing trigger if the acquisition is not busy with previous events. Since silicon trigger is faster, GMT could be in dead time from silicon trigger for the same event. Retriggering is avoided by delaying the $\overline{DT}$ signal by the time necessary for the electrons to arrive on the wires.

The Cathode pad signal:
For every event, a finite time is needed for complete charge collection on the cathode pads. This is done by delaying the readout of the GASSIPLEX, which is a low-noise analog signal processor that records the maximum amplitude of the charge induced in each pad and performs amplification, shaping and multiplexing. The recording is the aim of the Track and hold logic T&H [16].

The read out of the GASSIPLEX starts at the RDV (Retard et dare Variable) module which generates an ECL logic gate whose pulse width and delay time are adjustable. It is initiated both by a fired silicon signal delayed 10 μs to allow the electrons to drift to the wires and induce the charge on the cathode pads or by fired wire. RDV delay time is adjusted to 1.4 μs and generates a pulse 10 μs long. The gate produces T&H signal for the corresponding pads.

The delay imposed on the silicon (10 μs) and the OR logic of the wires intend to allow enough time for optimal collection of the charge on the pads before readout. While the width of the RDV pulse (10us) is made enough to hold the charge on the GASSIPLEX until the T&H signal overlaps with the readout signal coming from the OR logic gate of the wires. The GASSIPLEX then sends the information to the C-RAMS or CEAN readout for analog multiplexed signals.

The logic output signal from the RDV is used as well for time measurement as a common stop to the TDC, the start signal being the FTA signal from the GMT. A VETO signal inhibits the CFD form retriggering a T&H while the readout is being performed for the previous event.

CsI signal:
CsI scintillation detectors are used to make sure that particles escaping for the Si wall will be stopped and their energy is collected. Upon receiving a trigger at GMT, spectroscopy amplifier sends the charge collected in the PM tube to the acquisition system through the ADC.

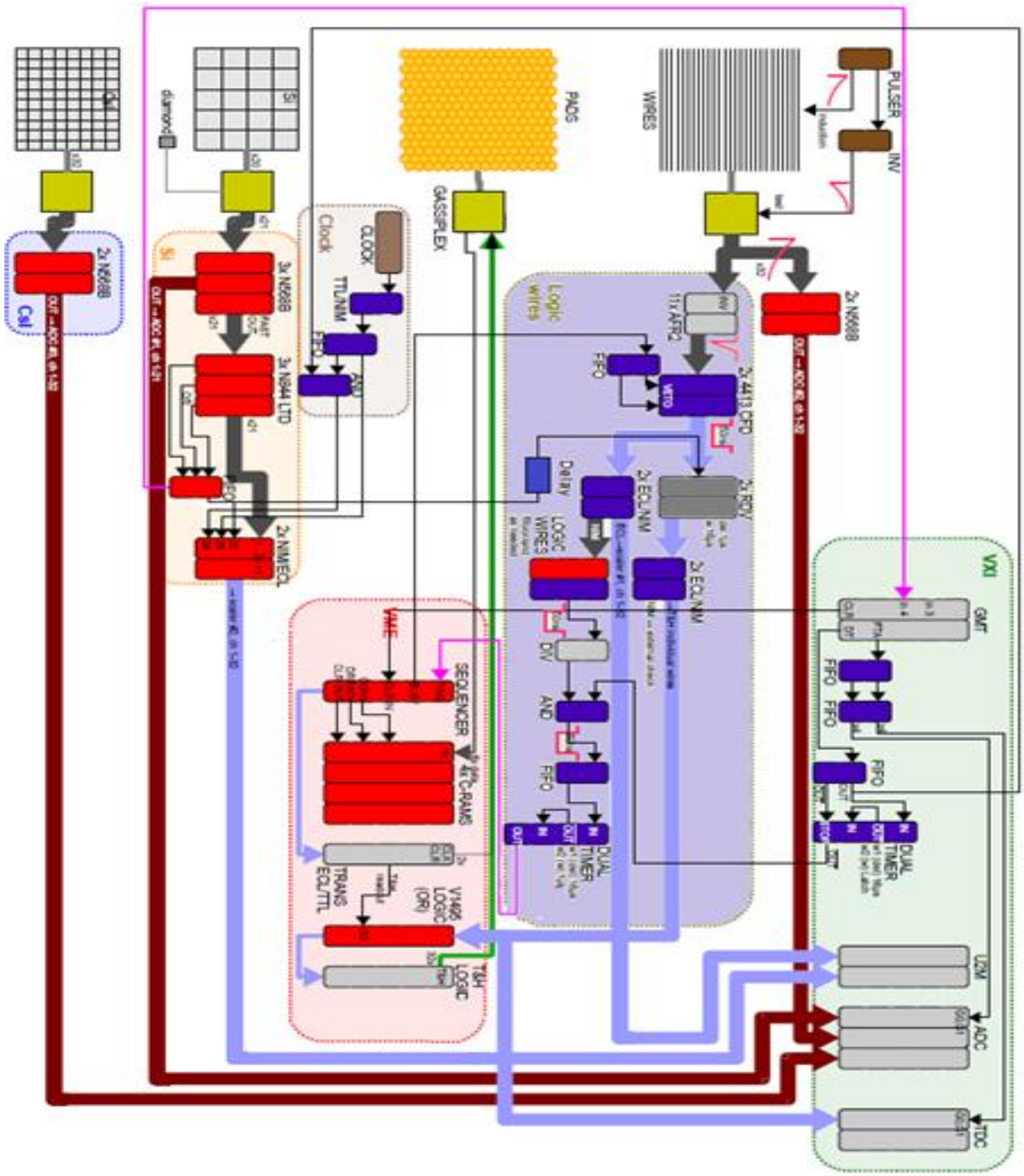

Figure 2.10 shows electronic scheme for Maya used in this experiment.

Chapter 3 Data Analysis

This chapter deals with the analysis of the data collected from the experiment performed at ISOLDE. Here we are concerned with the analysis of the events induced by ^{12}C present in the beam as a contamination. The ^{12}Be events are analyzed by S. Sambi (PhD student). The goal of this analysis is to prove the principle of the technique of elastic resonance scattering in inverse kinematic using Maya active target.

In the first part, calibration of various parts of the setup is described. Other components of Maya were calibrated in the course of the work on the ^{12}Be such as the cathode pads, anode wires and the CsI detectors. The results are used here directly. In section 3.2, particle identification is presented. Section 3.3 deals with the different methods to reconstruct the kinematics, and in section 3.4 its application to calculate the Q-value. At the end of the chapter, the ^{13}N-excitation function is discussed.

3.1 Calibration work

3.1.1 Drift Chamber energy calibration

The small drift chamber placed before the silicon wall serves as a ΔE-detector which provides identification of the reaction products in the E- ΔE technique. It is also used for reconstruction of the kinematics of the reaction as it used to localize the hitting point of the protons with a better resolution than the array of silicon detectors placed behind the chamber itself.

Energy calibration of the drift chamber depends on simulation of the energy loss of protons in the Maya filling gas. SRIM simulation code [25] is used to obtain the energy-range relation for protons shown in fig 3.1. This relation gives the range of a proton with a certain energy E in the gas at pressure 160 mbar.

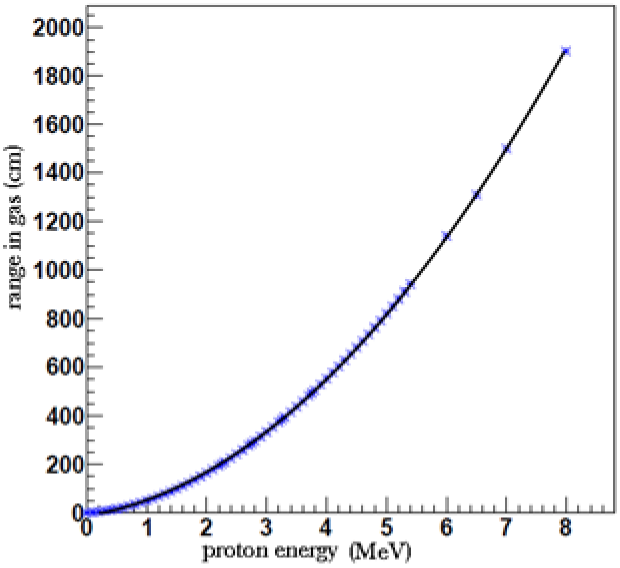

Figure 3.1 shows the energy of protons versus their ranges in the filling gas (isobutane).

This relation is used to find the energy loss in the drift chamber DC in the following way: assume an energy E is deposited in the silicon detector. The range corresponding to this energy is the distance that the proton would go further if the gas extended instead of the silicon wall. This range is extracted from the curve at E. Adding to this distance the gap between the silicon wall and the drift chamber, the same curve gives us directly the corresponding energy of the proton as it leaves the drift chamber.

In the same way, the energy of the protons entering the drift chamber is extracted from the curve at a distance equal to the width of the drift chamber plus the gap width. This distance should be measured from the range that corresponds to the proton energy E measured in the silicon. The energy loss in the drift chamber is the difference in proton energy entering and leaving the drift chamber. The energy loss ΔE for each event is plotted against the proton energy E deposited in the silicon to produce a theoretical E- ΔE plot as the one shown in fig. 3.2

Fig. 3.3 shows the experimental E-ΔE plot which gives the energy loss of light particles in the drift chamber measured by the anode wire in channels versus the energy measured by the central silicon detector. A cut was made in the experimental plot to select protons from the other light particles. The cut is shown in red. From proton events, an average kinematic line is constructed as the weighted average of the data for intervals of 100 keV on the energy measured in the silicon. The line is shown in fig. 3.3.

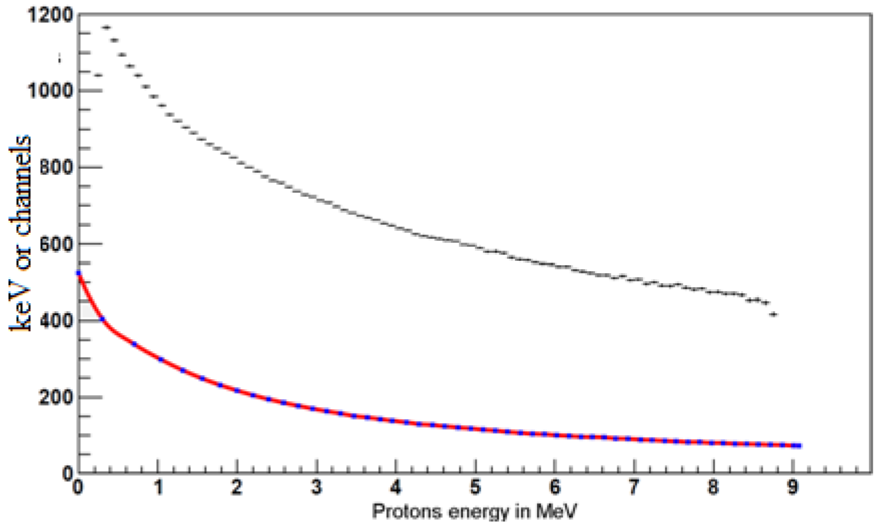

Figure 3.2 shows the theoretical kinematic line of the protons (red) and the experimental kinematic line in channels (black). The vertical scale is in keV for the red curve in channels for the black curve. See text for details about how the kinematic line was obtained.

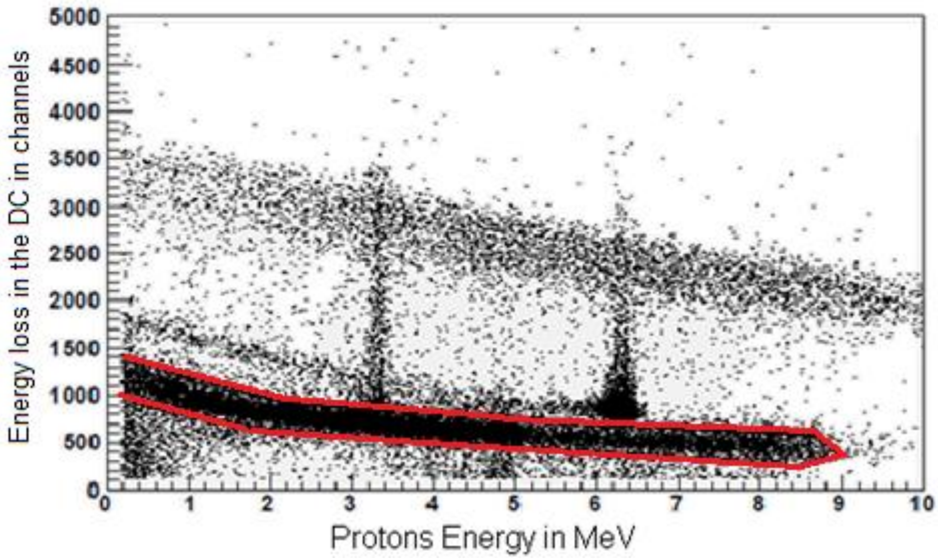

Figure 3.2 shows the experimental E- ΔE plot and the proton cut.

The calibration coefficients are obtained by fitting the theoretical line to the experimental one using a linear fitting function with an offset. The result of the fitting is shown in fig. 3.4 with the coefficients.

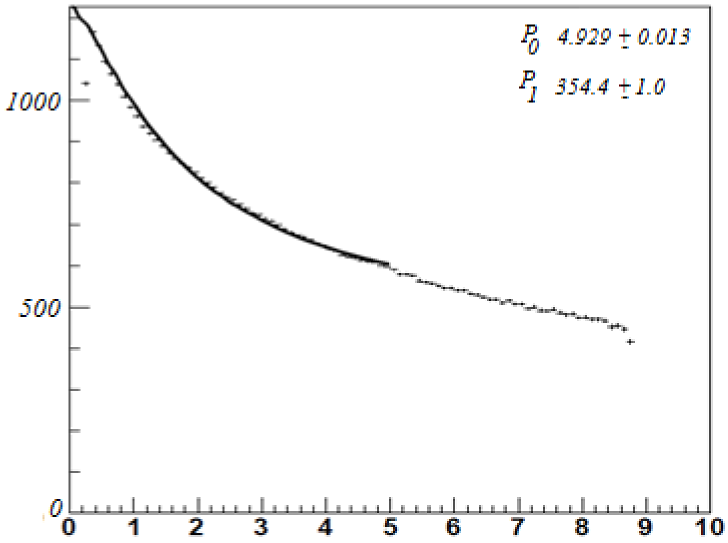

Figure 3.4 shows the fitting of the experimental curve with the theoretical one using a linear function and offset. The coefficients are given at the top right.

3.1.2 Drift chamber position calibration

The coordinates of the crossing point of the particle track in the drift chamber can be determined from the timing information of the signal collected at the anode wire.

Horizontal Position calibration

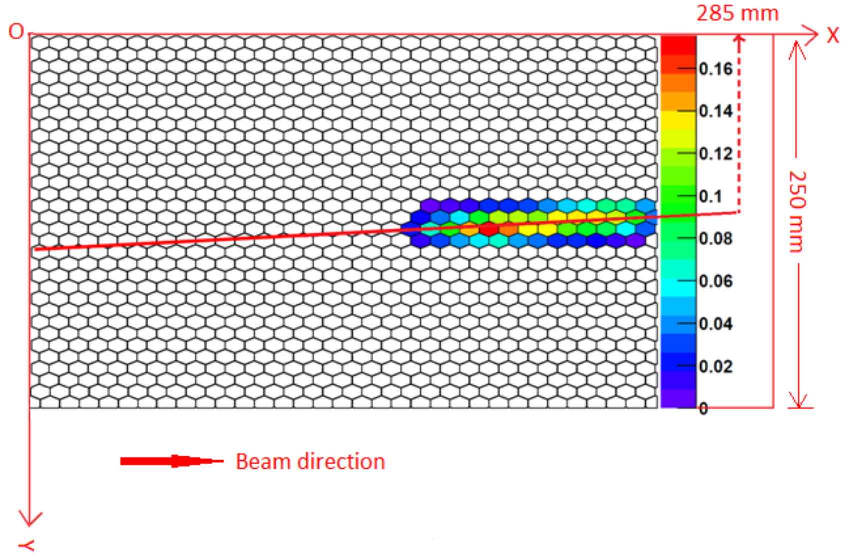

Figure 3.5 The origin of the coordinate system used to specify the indices of the crossing point in the drift chamber where the x-axis is along the beam that enters from the left and the y-axis is perpendicular to the beam direction. The figure shows a typical alpha particle track projection on the cathode pads.

The calibration of the horizontal or x-coordinate of the crossing point in the drift chamber makes use of patterns induced on the cathode pads in the main gas volume. The ionization track of a particle induces a pattern on the cathode pads. This pattern is a two dimensional projection of the particle track. To extract the direction of the 2-D induced pattern, a tracking algorithm is used. Two basic tracking methods namely the Hyperbolic Secant Squared and the Global Fitting method can be used. The details of these methods can be found in reference. The Global Fitting method was selected to obtain the fitting of the pattern which is a straight line as shown in fig. 3.5.

Calibration of the horizontal coordinate was performed with α-particles from a source located in the middle of the chamber. The chamber was filled with at a pressure of 50 mbar. This pressure is low enough to allow the α- particles to reach the silicon wall. This is to make sure that the particle has crossed the drift chamber. The patterns produced by the α-particles are then fitted with a straight line to obtain the x-coordinate of the crossing point.

The method of position sensing in the drift chamber depends on charge division. The charge created by ionization of the gas drifts towards the anode wire where it produces an avalanche. This charge from the avalanche is split into two signals towards both ends of the wire. The wire is fabricated such that it has a constant resistivity per unit length to provide a delay proportional to the length traveled by each charge to the corresponding end. The time intervals started by a trigger and ended by the arrival of the signal to the corresponding end is used to deduce the position of the avalanche, the horizontal projection of the crossing point.

These two times are referred to as the drift chamber left or right times; the position of the avalanche is proportional to the quantity $T_{DC\ left} - T_{DC\ right}$ .Plotting the horizontal position from the fitting of the pattern on the cathode pads versus this quantity, we obtain a straight line representing the conversion from channels to millimeters in our reference system. The results are shown in fig. 3.6.

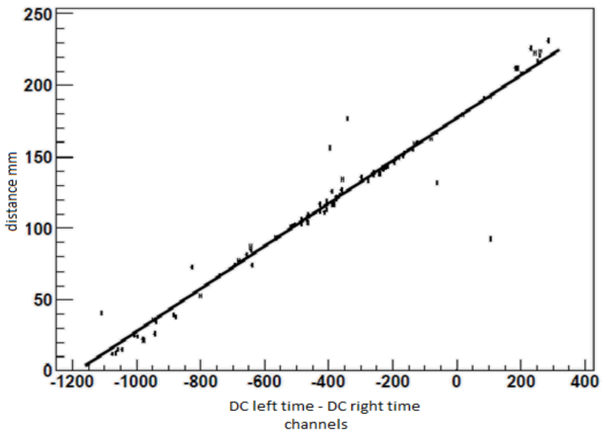

Figure 3.6 Results of plotting the difference in the drift time between left and right sides against the horizontal position calculated from the fitting of the particle track pattern on the cathode pads.

Vertical position calibration

Maya is based on the working principle of the time projection chamber TPC. The third dimension of the particle track is deduced from the drift times to the anode wires inside Maya. The ionization electrons drift with a constant velocity under the influence of a homogeneous electric field which makes the drift time proportional to the vertical distance.

The drift time of an anode wire is measured from the moment a signal arrives at that wire until a common stop signal of a fired silicon detector. As the silicon is triggered almost at the moment of the interaction, the silicon signal is suitably delayed to allow for all ionization electrons to reach the corresponding wires regardless where they were formed. This can be seen in the electronic scheme in fig. 2.9.

Drift times of neighboring wires can be fitted to a straight line whose slope is proportional to the slope of the particle track. Together with the projection of the track on the cathode pads, the 3D track can be reconstructed.

To calibrate the vertical position of the drift chamber, the z-coordinate of the crossing point is calculated by extrapolation of the particle track in the drift chamber and related to the DC anode time which is the time needed for the ionization electrons to drift to the wire. The recorded times were not properly set up during the experiment which forced the used of another quantity proportional to the vertical distance which is $T_{DC\ left} + T_{DC\ right}$ .These two drift times are defined as the time between the trigger and the arrival of the signal at the corresponding end, which makes the total time is proportional to twice the vertical distance.

The result of plotting the vertical distance obtained by track reconstruction in Maya and the time is shown in fig. 3.7. The fitting suffers from large spread especially near the ends and doesn’t exhibit a fully straight line. This is due to uncertainty of the fitting of drift times as well as small inhomogeneity of the field near the ends.

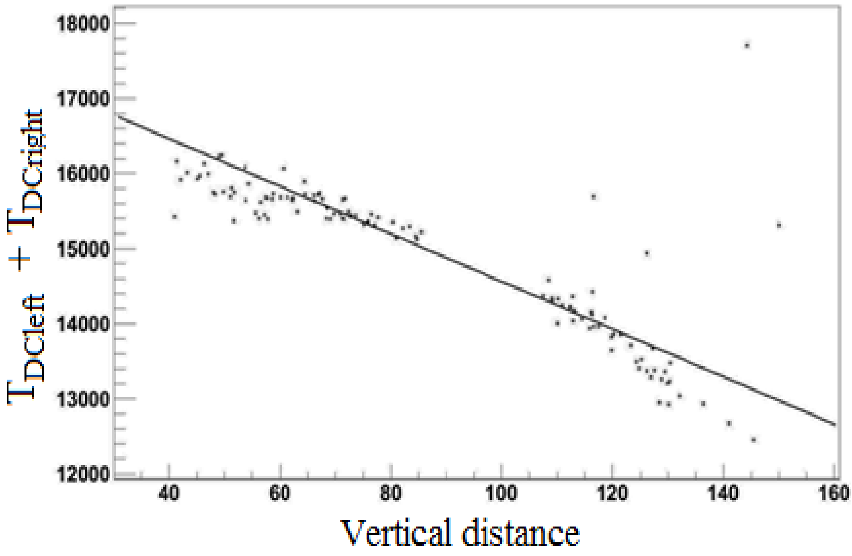

Figure 3.7 plotting the vertical distance against the quantity $T_{DC\ left} + T_{DC\ right}$

3.1.3 Silicon Detector Calibration

Energy calibration of the silicon wall detectors is performed using a standard alpha source placed on a movable arm in the middle of the chamber. The alpha source consisted of four α-emitters; ^{149}Gd, ^{239}Pu, ^{241}Am and ^{244}Cm. Except ^{149}Gd, these isotopes emit multiplets of α-particles close in energy. Their structure is given in table 3.1.

Table 3.1 Structure of the α-particles used in silicon calibration.

Isotope	Energy Mev	Intensity %
^{149}Gd	3.182	100
^{239}Pu	5.156	73.3
	5.144	15.1
	5.105	11.5
^{241}Am	5.485	85
	5.544	0.36
	5.442	13.3
^{244}Cm	5.804	76.4
	5.762	23.6

The gas chamber was kept under vacuum so that the α-particle deposits all of its energy in the silicon detectors. Each α-particle produces a peak in the detector which is in the ideal case Gaussian- shaped. However, it is noticed that there is a tail in the low energy side of the peaks which could be due to the energy loss of the α-particle before it leaves the source. These peaks were fitted to obtain the peak position which corresponds to the most probable energy. The calibration was done by plotting the tabulated energy of the α-particle versus the peak position. The plot is a straight line whose slope is the energy calibration coefficient.

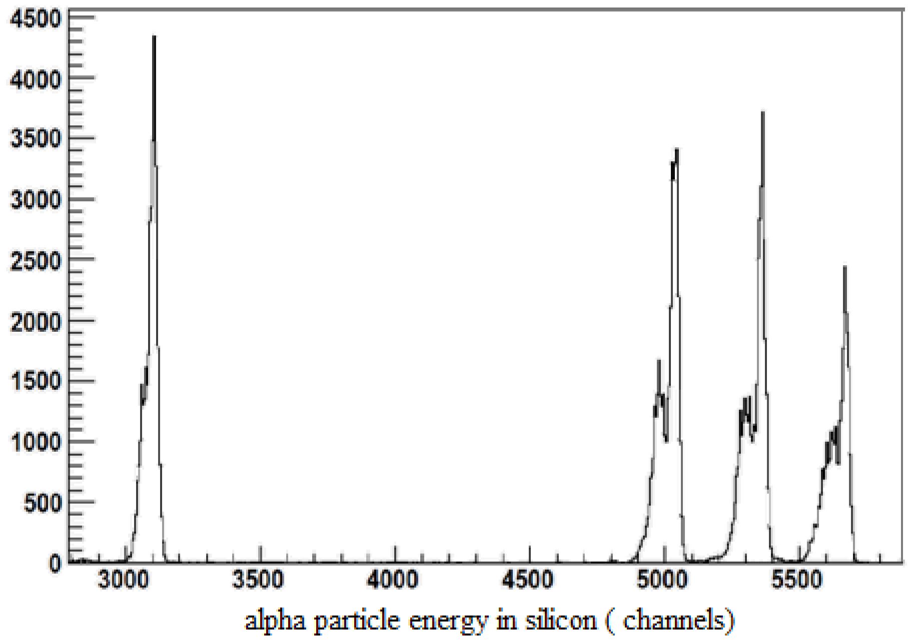

Figure 3.8a shows the response function of a high resolution detector. The peak on the left is ^{149}Gd which emits a single energy alpha. The tail effect is clear in this peak. The other peaks represent the ^{239}Pu, ^{241}Am and ^{244}Cm respectively. However, the structure can't be completely identified.

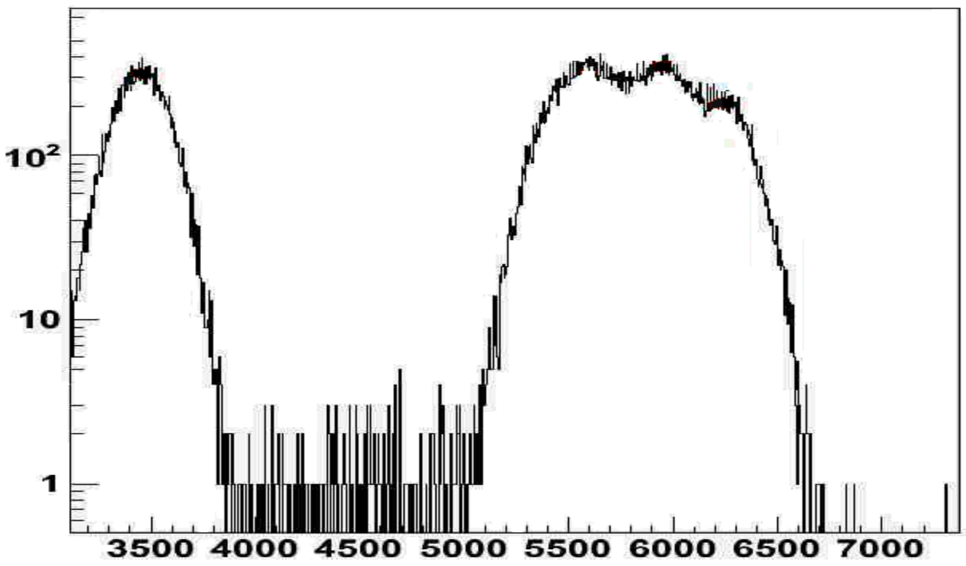

Figure 3.8b shows the response function of a poor resolution detector. The individual peaks corresponding to closely lying α-particles energies are merged in a single peak. In this case the position of this peak is plotted against the weighted average of α-particle energies.

The spectra of the alpha particles in silicon showed a large variation in the resolution of the silicon detectors. The poor resolution of the silicon detectors resulted in the merging of closely-lying α- particles peaks into a single peak. In most cases, the structure couldn't be completely identified. This is evident from comparing figures 3.8a and 3.8b, where the response functions for two different detectors are shown.

When individual peaks corresponding to different α-particles are merged in a single peak, the position of this peak is plotted against a weighted average energy calculated from the tabulated energy and intensity of each component in the peak.

3.2 Particle Identification

Different exit channels from the interaction of the beam with the gas were identified using the E-ΔE method. Using the central silicon detector opposite to the beam, we restrict the scattering angle to around 0 degree. The plot in fig. 3.9 shows the energy loss in the drift chamber in channels versus the energy in that silicon detector in MeV. The characteristic lines produced in the E-ΔE plot are footprints of the different light particles produced from the reactions.

The lowest parabola corresponds to protons. These protons are produced mainly from ^{12}C. SRIM simulation showed that these protons can reach the silicon wall only if they are produced in the first 10 cm of the ^{12}C range. Protons from ^{12}Be are superimposed on them.

Two vertical lines could be seen in the plot. These two lines are assumed to be contamination in the beam as this was not observed in any other detector except the central one. A further step in the identification is to put the energy loss in the drift chamber in energy units instead of channels to be able to compare it with the specific energy losses for light particles.

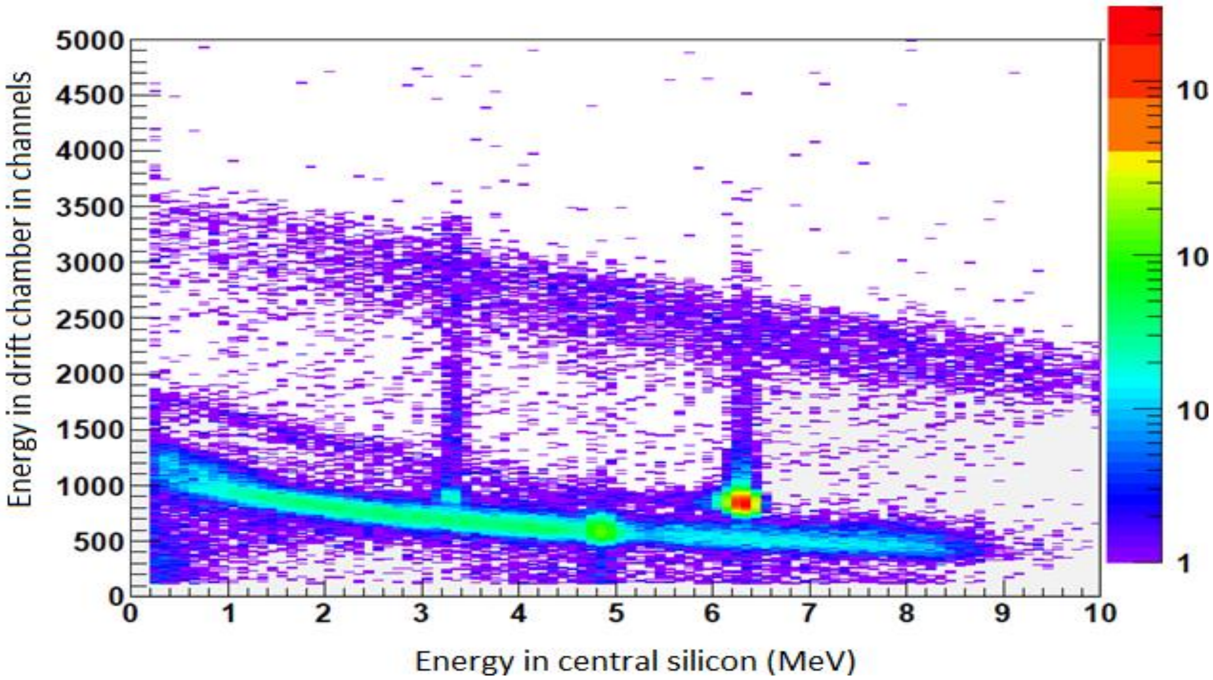

Figure 3.9 E-ΔE plot that is used for identification of particles produced by the reaction. The energy obtained by the silicon detector in MeV and the ΔE is given by the drift chamber in channels.

3.3 Reconstruction of the kinematics

Maya detector is designed for the study of binary reactions. Momentum conservation in binary reactions dictates that the incoming and outgoing particles lie in a single plane and the reaction products are scattered on a different sides with respect to the incident beam to conserve the momentum.

As mentioned before, the detector is capable of tracking the particle trajectory in three dimensions. The charge pattern induced on the cathode pads creates a two dimensional projection of the ionization track. This induced pattern is fitted to a straight line using a tracking algorithm. The vertex or the interaction point is the intersection of the straight line fitting the projected track with the beam line.

The third dimension or the vertical coordinate is deduced by three different methods: from the drift times on the anode wires in the active volume, from the crossing point of the particle track in the drift chamber and from the hitting point in the silicon.

Because energetic protons lost little energy in the filling gas of Maya, they didn't produce tracks on the cathode pads in many events. Also, our data had problems with the drift times on the anode wires and their fitting suffered from large uncertainty. Therefore, only available information from the drift times from the few good events were used to calibrate the drift chamber vertical coordinate. The vertical information is then restored by interpolation using the drift chamber vertical coordinates.

The crossing point in the drift chamber was also used with the vertex to produce the trajectory. The trajectory of a scattered proton is the straight line connecting the vertex and the crossing point. It was pointed out in the calibration section that the coordinates of the crossing point are deduced from the time information of the charge collected on the drift chamber DC anode wire.

However, these two methods suffer from large uncertainty stemming from uncertainty in the drift times on the anode wires of Maya in the first method or uncertainty in the drift time on the anode wire of the drift chamber for the second method. A reference method used to compare the above techniques is based on the dimension of the silicon detectors. The trajectory is obtained using the assumption that the hitting point of the proton is center of the triggered silicon. This introduces a fixed uncertainty to all events as it is limited by the spatial dimensions of the silicon detectors. This method however, provided the best results as will be shown in the results of the Q-value.

Once the trajectory is established, the reconstruction of the reaction kinematics is possible. This follows from the knowledge of the scattering angle ψ which is the solid angle between the beam line and the trajectory of the scattered particle. The projected angle φ is the angle on the cathode plane between the direction of the scattered particle, which is found by fitting the charge pattern with a straight line, and the beam direction. The polar angle θ is the angle between the trajectory and its projection in the horizontal plane containing the beam. The scattering solid angle can be calculated from the knowledge of these two angles by the trigonometry relation, shown in fig. 3.10.

$$cos\,\psi = \cos\,\theta\,\cos\varphi$$

Once the scattering angle is obtained, the energies of the particles after the interaction can be related to the energies of the reactants.

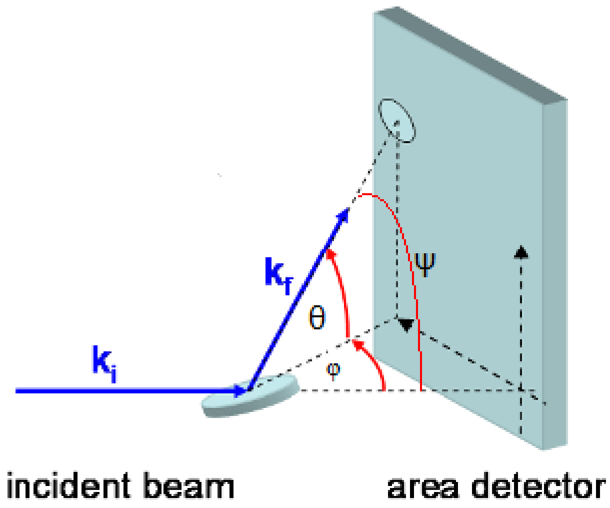

Figure 3.10: schematic drawing shows the geometry the geometry of the scattering angle

3.4 Q-value

Q-value is the difference in mass energies of the entrance channel particles and the exit channel particles. Consider a typical nuclear reaction a + X → Y + b, the Q-value is given by

$$\text{Q-value} = (m_a + m_X - m_b - m_Y)\,c^2 \qquad (1)$$

The Q-value can also be expressed in terms of the incoming and outgoing kinetic energies as

$$\text{Q-value} = (K_Y + K_b - K_a - K_X) \qquad (2)$$

When a beam of ^{12}C is scattered from protons, reactions that result in a proton in the exit channel include resonance scattering and direct[2] scattering. In a resonance scattering reaction, the quasi-bound state formed has only two modes of decay available: ejecting the particle elastically or in-elastically and subsequent γ-emission. The same recoil particles are produced. The Q-value therefore, is zero corresponding to an elastic scattering or negative corresponding to an inelastic scattering. This shows that Q-value could be used for identifying the elastic and inelastic events [1].

Discrimination between protons from ^{12}Be and ^{12}C is possible using the tracks on the cathode. Ionization pattern on the cathode pads after the mask is fitted to a straight line. These tracks were extrapolated to intersect with the beam line in the vertex or the interaction point. Proton tracks that produce a vertex after 12 cm belong to Be events. For tracks corresponding to a vertex in the first 12 cm, this could be for both ^{12}Be and ^{12}C. Since the ratio of ^{12}Be to ^{12}C in the beam is less than 1%, it is safe to neglect the contribution of ^{12}Be events.

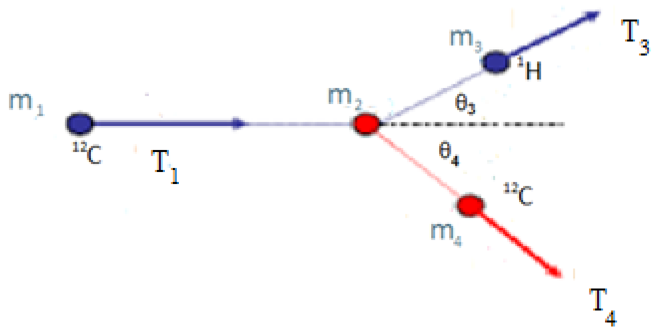

Figure 3.11: the two body kinematics of the scattering,

If the excitation energy of the ^{12}C after the scattering is zero, the scattering is elastic and the Q-value of the reaction is zero as well. In the relativistic description [26], the excitation energy of the nucleus of ^{12}C after scattering is given by

$$E_4^{exc} = m_4 - m_4^0 \tag{3}$$

Where m_4^0 is the rest mass energy of ^{12}C, and m_4 is given by the four vector relativistic formula

$$m_4^2 = E_4^2 - p_4^2 \tag{4}$$

Here, we used the convention $c = 1$ so masses should be substituted with the mass energies. E_4 is obtained by applying the conservation of total energy to the scattering shown in fig.2 The result is given by:

$$E_4 = T_1 + m_1 + m_2 - (T_3 + m_3) \tag{5}$$

[2] Called shape or potential scattering

The mass m_1 is the mass of the incident ^{12}C nucleus and m_2 (= m_3) is the mass of the scattered proton. T_1 is the kinetic energy of the ^{12}C nucleus at the point of interaction, and T_3 is the scattered proton kinetic energy.

Application of momentum conservation on the interaction gives the momentum of the ^{12}C or p_4 after the scattering as follows:

$$p_4^2 = p_1^2 + p_3^2 - 2p_1p_3\cos\psi_3 \qquad (6)$$

Again the subscripts 1and 3 refer to the momentum vectors of the ^{12}C before the interaction and the scattered proton after the interaction respectively. ψ_3 is the scattering angle of the proton.

Finally, the momenta in the last equation (6) can be related to the energies of the associated particles through the relation:

$$p = \sqrt{T^2 + 2Tm} \qquad (7)$$

The excitation energy of the ^{12}C nucleus requires the measurement of three variables. These are the energy of the incident ^{12}C beam T_1 , the energy of the scattered proton T_3 and the scattering angle ψ . The energies of the incident and scattered particles have to be measured at the point of interaction.

However, experimentally what is measured is the energy of the proton in the silicon wall after it has lost some energy in the gas. The energy lost in the gas is simulated for each event and added to the proton energy measured by the silicon. Also, the beam energy at the point of interaction is not given by the initial energy at the inlet of Maya. The ^{12}C nucleus loses about 1.36 MeV in the 2.5 um Mylar window. To correct for the energy loss in the gas, the stopping power of the ^{12}C nucleus was simulated using SRIM codes and the lost energy were subtracted from the beam energy on the basis of event by event.

Finally, the Q-value is calculated using two reconstruction techniques for the scattering angle in order to compare the results of these methods. The results are shown in fig 3.10a for scattering angles reconstructed using information of the vertex and the crossing point in the drift chamber and fig 3.10b for the vertex with the center of the silicon triggered by the proton. The peak is fitted with a Gaussian function. Peak position and the standard deviation of the peak are extracted.

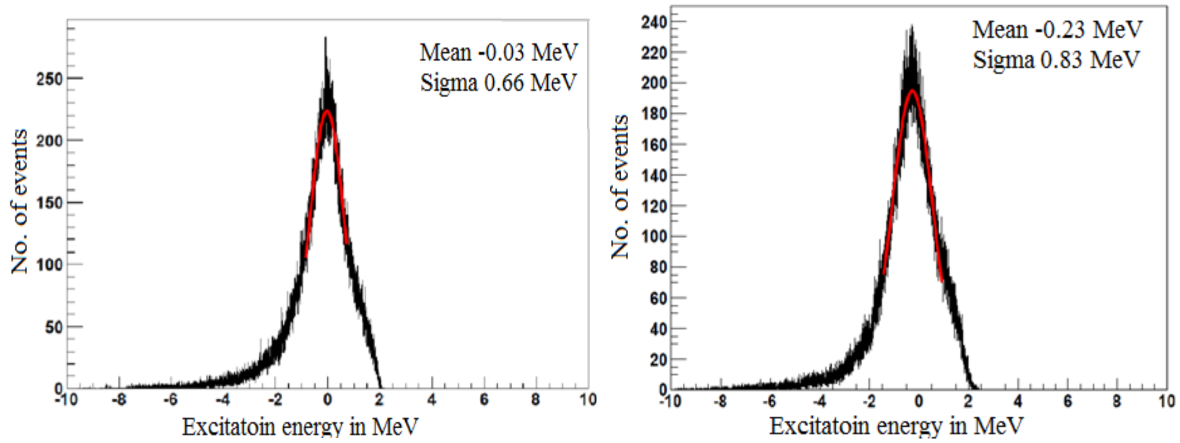

Figure 3.12 (right) shows the excitation energy using the drift chamber crossing point as the second point to reconstruct the scattering angle. (Left) shows the excitation energy using the center of the silicon point.

The figure shows that most of the events correspond to an elastic resonance scattering. This is because the excitation energy peak is centered around zero, which should be the case when the ^{12}C is left in the ground state after the scattering. The results show that the scattering angle reconstructed using the center of the silicon evidently improves the resolution. The tail in the negative side could be due to inelastic events at low energy excitation energy.

3.5 Estimation of Error

In order to account for the observed FWHM of the elastic peak in the excitation energy curve, the error in the observables entering the equation of the excitation energy should be specified. The main source of uncertainty is the vertex or the reaction point determination. Precise information about the energy of the ^{12}C nucleus at the interaction point is dependent on the position of the vertex. The specific energy loss of the protons is not constant and depends where the proton is produced. For these reasons, large error in the vertex will propagate to these observables and the broadening of the elastic peak is accounted for.

The origin of the vertex resolution is shown in fig. 3.13. When the angles of the scattered particle with respect to the beam axis are small (typically lower than 10 deg) or when its range is small (typically less than 5 cm), the uncertainty from the angle reconstruction has a strong influence on the resolution of the vertex position.

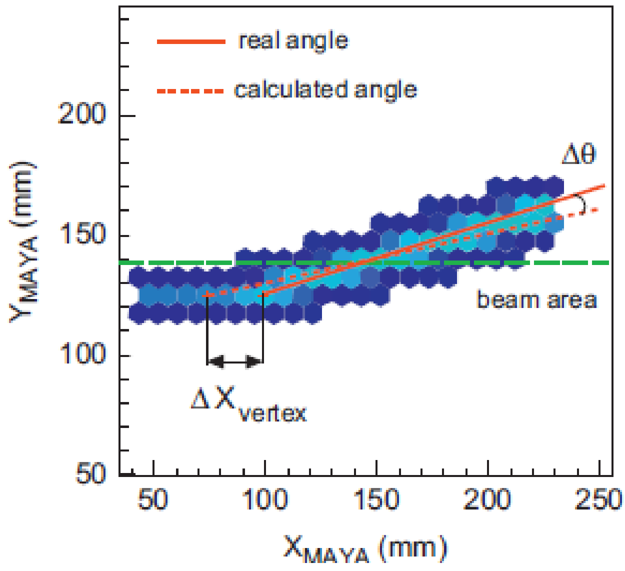

Figure 3.13 shows the origin of uncertainty in the vertex determination due to the angle reconstruction.

As a rough estimation, the order of magnitude of the uncertainty in the observables used to calculate the Q-value is deduced from the uncertainty in the vertex position. The uncertainty in the vertex determination was estimated using the resonant protons coming from the Carbon: fitting the traces corrisponding to the resonant peak in the silicons, the vertex distribution was broad with FWHM of 5 mm so the uncertainty in the vertex Δx = 5 mm.

ISOLDE beam enters Maya through a Mylar window which is a 2.5 um thick and can withstand a pressure up to 250 mbar. The energy loss due to the Mylar was estimated to be 1.36 MeV for ^{12}C using SRIM.

Assuming that the specific energy loss is constant within the 5 mm distance corresponding to the uncertainty in the vertex, the corresponding uncertainty in the ^{12}C energy, $\delta E(^{12}\mathrm{C})$ is given by :

$$\delta E(^{12}\mathrm{C}) = \Delta x \times \frac{dE}{dx}$$

where $\frac{dE}{dx}$ is the specific energy loss of the ^{12}C. Specific energy loss for the ^{12}C at the point of interaction is obtained from SRIM simulation. It varies between 0.192 MeV/mm near the entrance to 0.455 MeV/mm at the Bragg beak. This corresponds to 0.96 MeV and 2.28 MeV respectively. This uncertainty will be present in the terms containing T_1 or P_1 in equations (5) and (6) and accounts for the large FWHM observed.

The uncertainty in the proton energy $\delta E(^{1}\mathrm{H})$ due to uncertainty in the vertex is small compared to that of the ^{12}C because the energy loss for protons occurs at the beginning of their tracks. The specific energy loss for proton $\frac{dE}{dx}$ depends on the square of the atomic number z^2 (Bethe-Bloch formula) which also makes the order of magnitude of the uncertainty in proton energy $\delta E(^{1}\mathrm{H})$, 36 times less than that of carbon.

3.6 Excitation function of ^{13}N

The low-lying resonances in ^{13}N are well known from many previous experiments that used different techniques since the ^{13}N nucleus could be easily reached using stable target of ^{12}C[27].

One experiment that uses elastic resonance scattering and a thick gas target is given in the paper of K. Markenroth *et al*. It exploited the resonance in ^{13}N to perform a calibration for the silicon detectors and at the same time a performance check for the setup. In this experiment, a ^{12}C beam was scattered on methane gas at a pressure about 240 mbar. This pressure was enough to stop the beam before the silicon detector placed at 0^{o} lab angle. This allows measurement at this angle which corresponds to 180^{o} degrees in the center of mass. At this angle, coulomb and potential scattering which interfere with elastic scattering is minimal. Figure 3.13 gives the excitation function of ^{13}N. The excitation function shows one peak that is attributed to the two closely lying resonances at 3.50 and 3.55 MeV. The resonance state +1/2 at 420 keV above the proton emission threshold in ^{13}N is not seen in the spectrum because coulomb scattering dominates below 0.5 MeV.

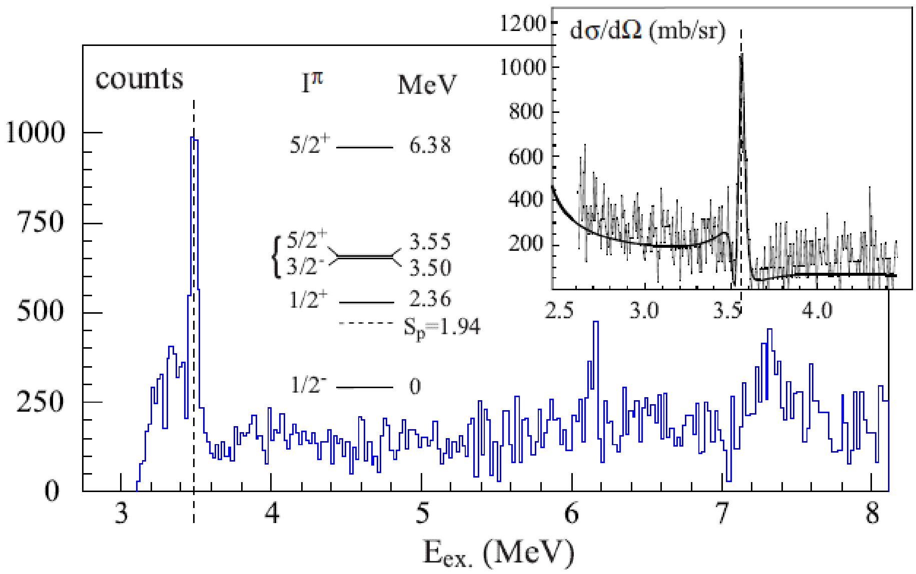

Figure 3.14: (blue) the excitation function of ^{13}N as measured by ^{12}C+ *p* elastic scattering in a thick gas target in inverse kinematics. The figure shows a schematic view of ^{13}N and the inset shows the part at the doublet. The resonances are fitted using two peaks added coherently to take interference into account [2].

3.7 ^{13}N results from Maya

The goal of this work is to use the ^{12}C scattering on protons in Maya for the proof of the principle of resonance elastic scattering in inverse kinematics using Maya active target detectors. The reconstruction of the tracks enables us to measure at angles outside the 180^0 in the center of mass. Thereby increasing the statistics compared to other techniques using thick targets.

Protons from ^{12}C come from interaction occurring in the first 12 cm in the gas, this is the range of the ^{12}C ions in the gas at the pressure used. These protons are selected by imposing the condition on the vertex of the interaction to be located in the first 12 cm. Although ^{12}Be interaction could occur within this range, the statistics are extremely low to affect ^{12}C spectra.

The ancillary wall covers a solid angle of 45^0 around the beam for events in the middle of Maya (15 cm). Since scattering in inverse kinematics brings forwardly focused protons to the silicon detector wall, this increases the detection efficiency.

The proton spectra in the lab frame are shown in fig. 3.15. In this figure, the spectra in all the 20 silicon detectors comprising the ancillary wall are viewed. The lap spectra show the energy in the silicon in MeV versus the number of counts. The inverse kinematic effect is evident in the figure since only the detectors facing the narrow cone around the beam has much higher statistics. The proton spectra end at 5 MeV due to a cut made in the analysis to include the energies up to the resonance at around 4.8 MeV in the lap. A similar cut was made at low energies to exclude the events due to coulomb scattering which dominates below 0.5 MeV [17].

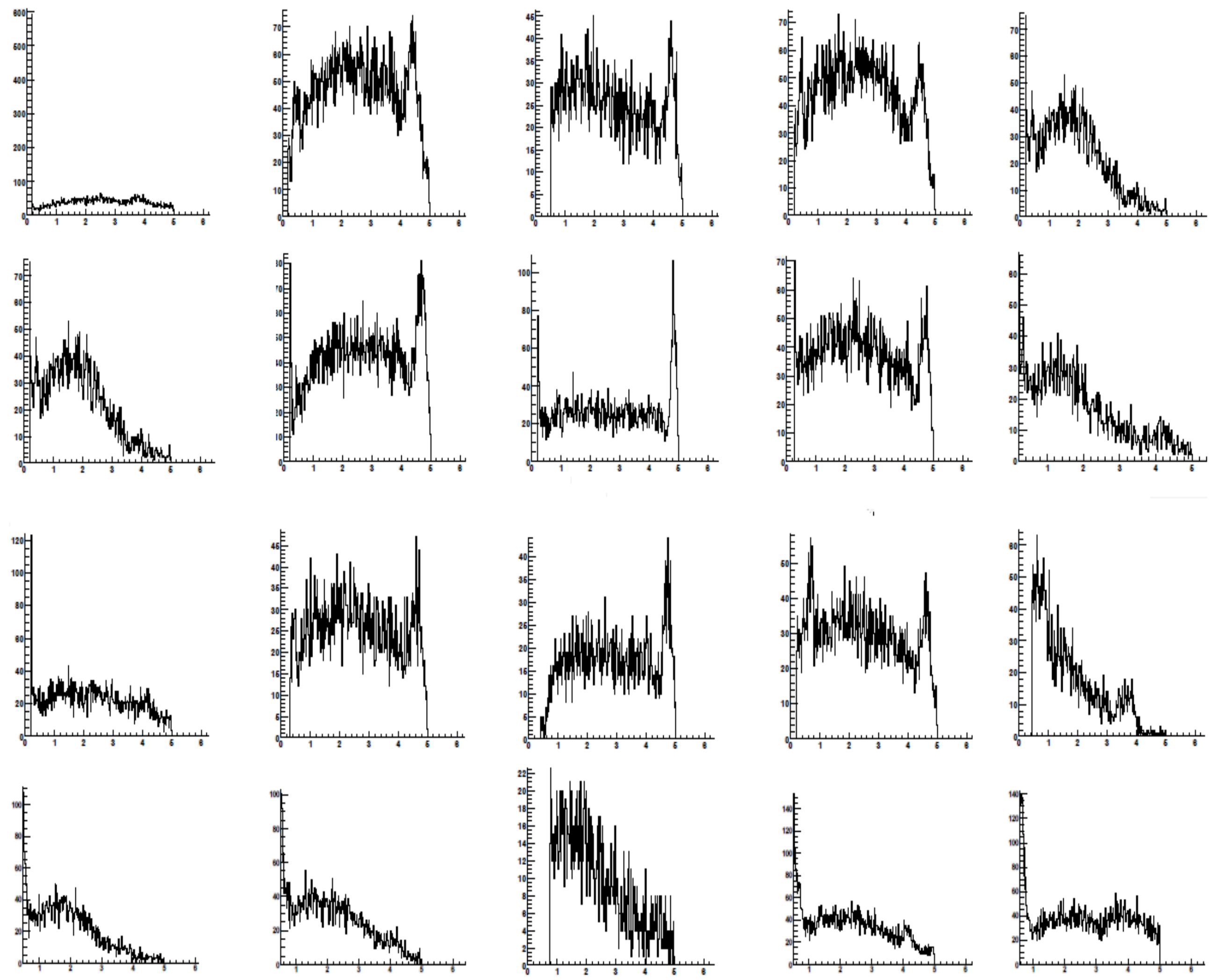

Figure 3.15: the lap spectra as recorded by the silicon wall detectors. The horizontal axis is the energy in the lab versus the number of counts.

The transformation to the center of mass system [17] is done by considering the total kinetic energy after the scattering in the center of mass system which is given by:

$$E_f^{'} = E_i^{'} + Q \quad (13)$$

where $E_i^{'}$ is the total kinetic energy in the center of mass before the scattering and Q is the Q-vlaue of the reaction. Since most of the interactions corresponded to elastic scattering, then $Q = 0$, and $E_f^{'} = E_i^{'}$. This was seen from the Q-value curves. The tail in the negative side corresponding to inelastic events is much less than the elastic peak. The total kinetic energy is given by:

$$E_i^{'} = E_c \frac{M_c}{M_c+M_p} = \frac{1}{13} E_c \quad (14)$$

Where E_c is the energy of the ^{12}C nucleus at the point of interaction. M_c and M_p are the masses for the ^{12}C and the proton respectively. E_c is given in terms of the proton energy measured in the silicon and the scattering angle by the equation

$$E_c = \frac{(M_c+M_p)^2}{4M_cM_p cos^2\psi} E_p \tag{15}$$

Here E_p is the proton energy after the scattering and ψ is the scattering angle.

The excitation function for ^{13}N in the center of mass was obtained using the scattering angle ψ that is reconstructed from the information of the vertex and the center point of the triggered silicon detector. The crossing point in the drift chamber, due to bad resolution didn't result in identifiable resonance.

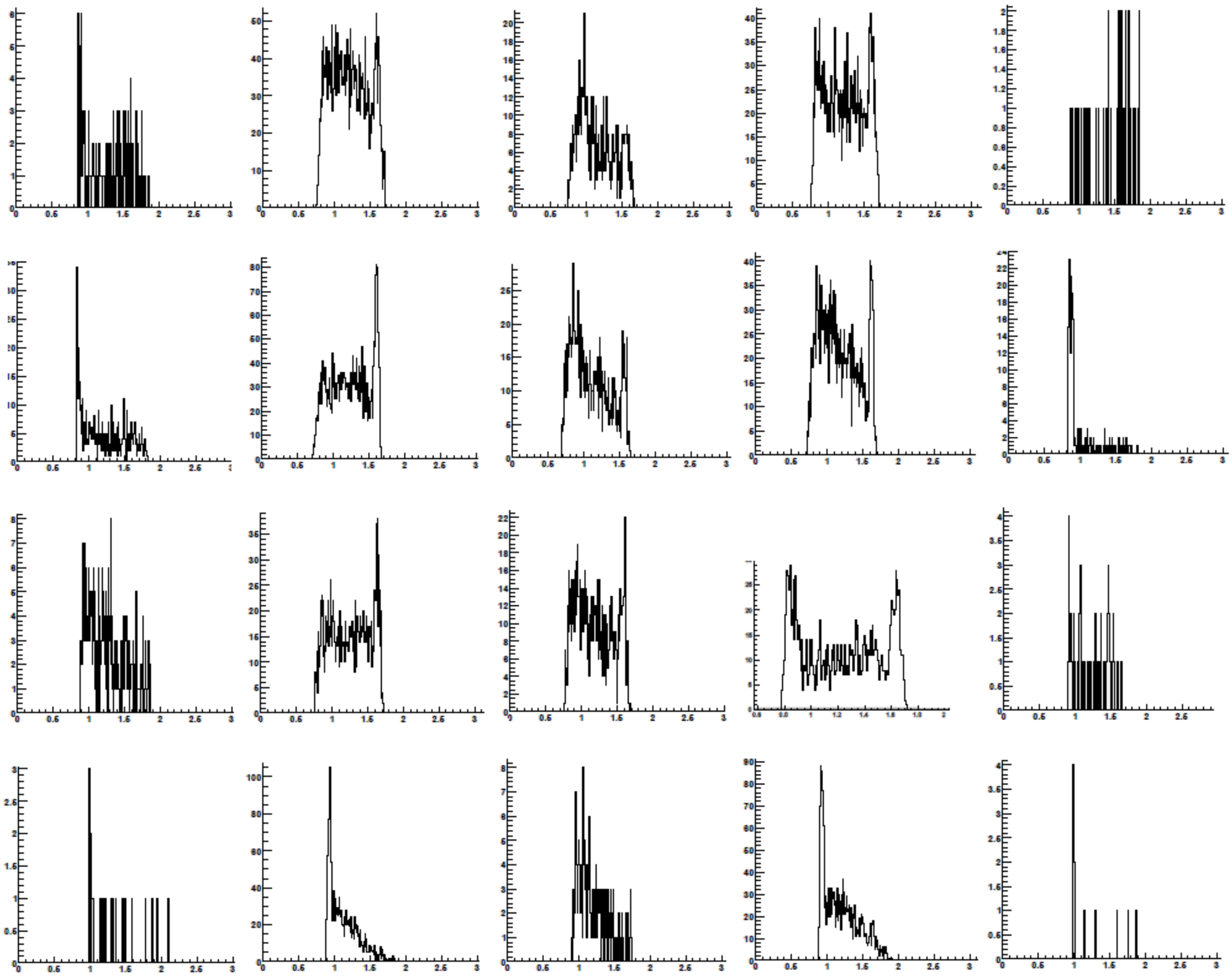

Figure 16: the center of mass spectra shows the doublet resonance.

The excitation function of ^{13}N is obtained here by reconstruction of the kinematics through tracking the trajectory of the scattered proton and the vertex. The advantage of this technique is that it allows the measurement outside 180^0 while covering large solid angle. Inverse kinematics adds to this advantage as most of the events are forwardly focused.

Therefore, statistics are well improved. The sum up of all the events in the silicon detector wall is given in fig. 3.17.

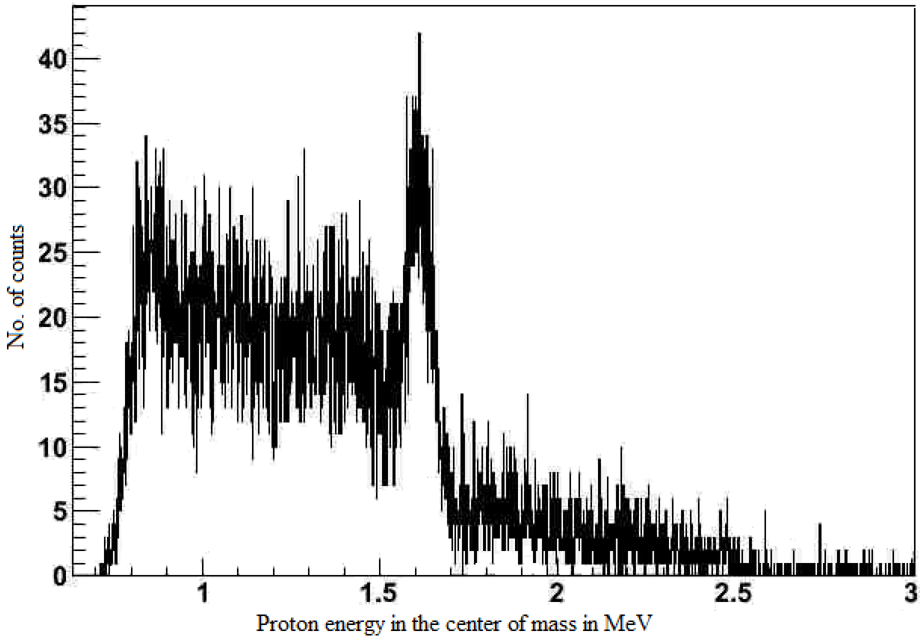

Figure 3.17: The excitation function of ^{13}N in the center of mass obtained by summing the events in all the silicon detectors.

Conclusion

This work intends to demonstrate the technique of elastic resonance scattering in inverse kinematics using the Maya active target. This technique provides several experimental advantages. The use of Maya active target allows the 3D tracking of the recoil particles trajectory. This information is necessary for the reconstruction the kinematics of the scattering. The tracking of trajectory made it possible for the measurement at angles outside 180^0 which improves the statistics significantly.

Once the kinematics is known, separation between elastic and inelastic events as well as the observation of ^{13}N resonance peaks in the excitation function is possible. The excitation energy of the ^{12}C after scattering showed a broad elastic peak with a tail corresponding to inelastic events. The excitation function showed the two closely lying resonant peaks at 3.50 and 3.55 MeV.

The Maya detector perfectly suits experiments where low counting rate is involved. Therefore, the high counting rate of the ^{12}C affected the measurement and a modification to the setup has to be made to be able to trigger on the interesting ^{12}Be events and avoid the paralysis of the acquisition system. ^{12}Be -induced events will have to be carefully filtered out applying coincidence conditions.

The use of a small drift chamber before the silicon wall aimed at improving the localization of the hitting point of the protons with a better spatial resolution than the array of silicon detectors behind it. However, due to problems with the data, an accurate calibration of the coordinates of the drift chamber was difficult. This affected greatly the resolution with which the reconstruction of the trajectories was made.

Maya active target has proved to be a valid tool in detecting and measuring reaction observables. This initiated the project to design a new active target detector called ACTAR [28] that further improves the data acquisition and fitting algorithms in Maya.ng algorithms in Maya

References

[1] K.S. Krane. *Introduction to Nuclear Physics*. John Wiley & Sons, 1988.

[2] K. Markenroth. *Exploring the exotic, experimental investigations far from stability*. PhD thesis, Chalmers university of technology and Goteborg university, Sweden, 2001.

[3] P. G. Hansen, B. Jonson. *Euro. Lett.* , 4(4), (1987) 409.

[4] K Riisager, Halos and related structures , Phys. Scr. T152 (2013) 014001.

[5] T. Otsuka et al., Phys. Rev. Lett. 87 (2001) 082502.

[6] D. Guillemaud-M¨uller et al., Nucl. Phys. A426(1984) 37.

[7] Magdalena Kowalska, *Ground state properties of neutron-rich Mgisotopes – the "island of inversion" studied with laser and β-NMR spectroscopy,* PhD thesis, Mainz, 2006.

[8] J. R. Terry, B. A. Brown, C. M. Campbell, J. M. Cook, A. D. Davies, D.-C. Dinca, A. Gade, T. Glasmacher, P. G. Hansen, B. M. Sherrill, and H. Zwahlen. Phys. Rev. C 77, 014316 (2008).

[9] Kris Heyde, John L. Wood, REVIEWS OF MODERN PHYSICS, VOLUME 83, OCTOBER–DECEMBER 2011

[10] B. Blank, M.J.G. Borge, Nuclear structure at the proton drip line: Advances with nuclear decay studies. Progress in Particle and Nuclear Physics 60 (2008) 403–483.

[11] Manuel Caamãno Fresco. *Production and characterization of the ^{7}H resonance*. PhD thesis, Universidade de Santiago de Compostela,2006.

[12] R. Raabe, T. Roger, M. J. G. Borge, M. Caamaãno, D. Cortina-Gil, F. de Oliveira Santos, B. Fernandez-Dominguez, M. Freer, H. O. U. Fynbo, L. Gaudefroy, J. Gibelin, G. F. Gryner, A. Heinz, J. S. Johansen, B. Jonson, M. Marques, W. Mittig, E. N_acher, T. Nilsson, G. Nyman, N. Orr, E. Pollacco, K. Riisager, P. Roussel-Chomaz, S. Sambi, H. Savajols, O. Tengblad,
M. Vandebrouck, H. Wang. *Study of ^{13}Be through isobaric analog resonances in the Maya active target*. Proposal to the ISOLDE and Neutron Time-of-Flight Committee,2011.

[13] I. J. Thompson and M. V. Zhukov, Phys. Rev. C 53, 708 (1996).

[14] V. Z. Goldberg, in Exotic nuclei and atomic masses (ENAM 98) (AIP Conference Proceedings, 1998), Vol. 455, p. 319.

[15] G. V. Rogachev et al., Phys. Rev. C 67, 041603 (2003).

[16] Domenico Torresi, *Excitation of Unbound States in ^{12}B Via the ^{8}Li-Resonant Elastic Scattering*. PhD thesis, UNIVERSITA DEGLI STUDI DI CATANIA, 2010.

[17] K. Markenroth, L. Axelsson, S. Baxter, M. J. G. Borge, C. Donzaud, S. Fayans, H. O. U. Fynbo, V. Z. Goldberg, S. Grévy, D. Guillemaud-Mueller, B. Jonson, K.-M. Kallman, S. Leenhardt, M. Lewitowicz, T. Lonnroth, P. Manngard, I. Martel, A. C. Mueller, I. Mukha, T. Nilsson, G. Nyman, N. A. Orr, K. Riisager, G. V. Rogachev, M.-G. Saint-Laurent, I. N. Serikov, N. B. Shul'gina, O. Sorlin, M. Steiner, O. Tengblad, M. Thoennessen, E. Tryggestad, W. H. Trzaska, F. Wenander, J. S. Winfield, and R. Wolski. *Crossing the dripline to ^{11}N using elastic resonance scattering*. PHYSICAL REVIEW C, VOLUME 62, 034308.

[18] Piet Van Duppen. *Isotope online separation and post acceleration*. Lecture notes, Instituut voor Kern- en Stralingsfyisca, K. U. Leuven, 3001 Leuven, Belgium

[19] Www. Isolde.web.cern.ch

[20] C.E. Demonchy, *et al*. MAYA*: An active-target detector for binary reactions with exotic beams*. Nuclear Instruments and Methods in Physics Research A 583 (2007) 341–349.

[21]C.E. Demonchy, W. Mittig, H. Savajols, P. Roussel-Chomaz, M. Chartier, B. Jurado, L. Giot, D. Cortina-Gil, M. Caamãno Fresco, G. Ter-Arkopian, A. Fomichev, A. Rodin, M.S. Golovkov, S. Stepantsov, A. Gillibert, E. Pollacco, A. Obertelli, H. Wang. *Maya, a gaseous active target*. Nuclear Instruments and Methods in Physics Research A 573 (2007) 145–148.

[22] Y. Mizoi, T. Fukuda, Y. Matsuyama, T. Miyachi, J. Nakano, N. Fukuda, M. Hirai, H. Kobinata, Y. X. Watanab, H. Sakurai, Y. Watanabe, A. Yoshida. *Multiple-sampling and tracking proportional chamber for nuclear reactions with low-energy radioactive isotope beams*. Nuclear Instruments and Methods in Physics Research A 431 (1999) 112}122.

[23] T. Roger, M.Caamanão , C.E.Demonchy , W.Mittig , H.Savajols , I.Tanihata. *Tracking algorithm for the active target Maya*. Nuclear Instruments and Methods in Physics Research A 638 (2011) 134–142.

[24] A.C.C. Villari and the SPIRAL group Nucl. Instrum. Methods B204 (2003)31.

[25] James Zeigler ,www.srim.org

[26] F. Flavigny, Determination de facteurs spectroscopiques absolus par reactions de knockout et de transfert. PhD thesis, 2011.

[27] F. Ajzenberg-Selove, Nuclear Physics A523 (1991).

[28] http://www.usc.es/genp/actar/

[29] M. Caamanão, D. Cortina-Gil, W. Mittig, H. Savajols, M. Chartier, C. E. Demonchy, B. Fernaãndez, M. B. GÓmez Hornillos, A. Gillibert, B. Jurado, O. Kiselev, R. Lemmon, A. Obertelli, F. Rejmund, M. Rejmund, P. Roussel-Chomaz, and R. Wolski. *resonance state in ^{7}H.*

[30] G.F. Knoll. *Radiation Detection and Measurement*. John Wiley & Sons, 2000.

[31] D.J. Morrissey and B.M. Sherill, In-flight Separation of Projectile Fragments, Lect. Notes Phys. 651, 113–135 (2004).

[32] Y Blumenfeld, T Nilsson, and P Van Duppen, Facilities and methods for radioactive ion beam production. Phys. Scr. T152 (2013) 014023.

AFDELING
Straat nr bus 0000
3000 LEUVEN, BELGIË
tel. + 32 16 00 00 00
fax + 32 16 00 00 00
@kuleuven.be
www.kuleuven.be